



Application of photoelectron holographic imaging to the study of Si(100) interfacial structures
by Mickey Hong Yu

A thesis submitted in partial fulfillment of the requirements for the degree of Doctor of Philosophy in
Physics

Montana State University

© Copyright by Mickey Hong Yu (1995)

Abstract:

It has always been one of the major goals in surface science to experimentally determine surface and interface structures. It has been demonstrated, in this thesis work, that three-dimensional images of the surface and interface structures can be obtained directly by means of photoelectron holography without any model calculations.

In the application of photoelectron holography to the study of the technologically important semiconductor interfaces, three systems have been chosen, Si(100)-Se:1x1, Si(100)-Al:2x2, and Si(100)-Mg:2x2. Of the three systems studied, selenium adsorbates are found to occupy the bridge sites. Selenium adsorbates have totally removed the reconstruction formed by surface silicon atoms, and the silicon surface is changed from single-domain to double-domain under the influence of selenium atoms, which implies that selenium atoms react with the silicon surface and etching occurs during the adsorption process. Aluminum on Si(100) has been a long-standing issue regarding the orientation of Al ad-dimers with respect to the underlying Si dimers. Photoelectron holographic imaging results of Si(100)-Al:2x2 clearly show that Al adsorbates form parallel ad-dimers. This is first time that photoelectron holographic imaging technique has been applied to a totally unexplored system, Si(100)-Mg:2x2. The image results successfully show that magnesium adsorbates occupy the four-fold hollow sites. In conjunction with LEED study, an interfacial structure is obtained.

APPLICATION OF PHOTOELECTRON HOLOGRAPHIC IMAGING TO THE
STUDY OF Si(100) INTERFACIAL STRUCTURES

by

Mickey Hong Yu

A thesis submitted in partial fulfillment
of the requirements for the degree

of

Doctor of Philosophy

in

Physics

MONTANA STATE UNIVERSITY-BOZEMAN
Bozeman, Montana

September 1995

D378
4906

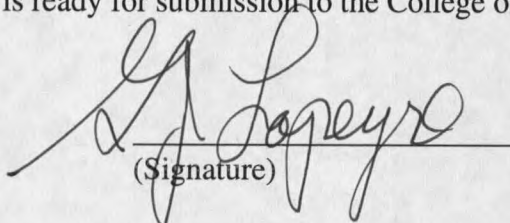
APPROVAL

of a thesis submitted by

Mickey Hong Yu

This thesis has been read by each member of the thesis committee and has been found to be satisfactory regarding content, English usage, format, citations, bibliographic style, and consistency, and is ready for submission to the College of Graduate Studies.

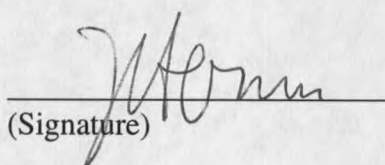
Dr. Gerald J. Lapeyre


(Signature)

9/1/95
Date

Approved for the Department of Physics

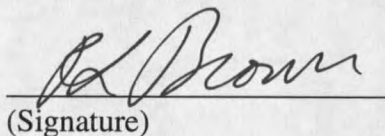
Dr. John C. Hermanson


(Signature)

9-1-95
Date

Approved for the College of Graduate Studies

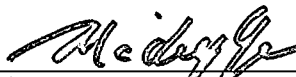
Dr. Robert L. Brown


(Signature)

11/13/95
Date

STATEMENT OF PERMISSION TO USE

In presenting this thesis in partial fulfillment of the requirements for a doctoral degree at Montana State University-Bozeman, I agree that the Library shall make it available to borrowers under rules of the Library. I further agree that copying of this thesis is allowable only for scholarly purposes, consistent with "fair use" as prescribed in the U.S. Copyright Law. Requests for extensive copying or reproduction of this thesis should be referred to University Microfilms International, 300 North Zeeb Road, Ann Arbor, Michigan 48106, to whom I have granted "the exclusive right to reproduce and distribute my dissertation in and from microform along with the non-exclusive right to reproduce and distribute my abstract in any format in whole or in part."

Signature 

Date 9/11/95

to my ever supportive parents to whom I owe everything, to my dear wife who has given me everything, and to my lovely daughter to whom I shall give everything

VITA

The author was born on November 11, 1960 in Beijing, China. He is the eldest of Z. X. Yu and L. S. Ming and has two younger brothers, Tao Yu and Bo Yu. He married Ms. Hong Zhao in 1986 and has one daughter, Christina Yanie Yu, who was born in Bozeman, Montana on October 10, 1992.

The author successfully finished his undergraduate study with a B.Sc. in Physics at Beijing Normal University in 1983. He successively went on his graduate study at the same school and obtained an M.Sc. in Material Science. Later, he worked in the Institute of Physics, Chinese Academy of Sciences for more than three years before he came to the United States pursuing Ph.D in Physics Department, Montana State University with his advisor Dr. G. J. Lapeyre.

ACKNOWLEDGMENTS

I would like to thank my advisor Dr. G. J. Lapeyre for his constant support, instructive advice, and inspiring encouragement over the past six years. His untiring pursuit for science has set an example for me.

I would like to express my heartfelt gratitude to Dr. J. R. Anderson. I still remember the first time we met in China, and the days we spent together. His technical advice is an invaluable asset to my career. His critical reading of this thesis is especially appreciated.

My cordial thanks go to Dr. J. C. Hermanson for his great help and care at the most difficult times in my life. I am also grateful to him for the fruitful discussions about quantum mechanics, which benefited me a great deal in the thesis writing.

I would also like to thank Dr. C. Olson from Iowa State University for his great help in the use of synchrotron facilities. Many thanks to Dr. H. Wu for many helpful discussions with him about photoelectron holography, and to Dr. L. Zhu and J. Wu for their help at the Synchrotron Radiation Center. Life would've been much tougher without their company. Erik Andersen and Norm Williams, your help will always be remembered.

There are so many people I'd like to thank, from whom I have benefited in the past six years. All in all, I'd like to say to all of you, Thank you very much!

Finally, I'd like to thank my wife Hong. I wouldn't have gone through all this without her company and support. And thank you Christina, my lovely daughter. You make my life full of sunshine!

TABLE OF CONTENTS

	Page
1. INTRODUCTION	1
Photoelectron Holography and its Development.....	1
Purposes and Motivations of the Present Work	3
Review of Previous Studies of Se, Al and Mg on Si(100) Surfaces.....	4
Structure of the Paper.....	5
2. THEORY	7
Principles of Photoemission.....	7
Photoemission Phenomenon and the Three-Step Model.....	7
Quantum Mechanical Description of Photoemission Process.....	10
Single-Atom System.....	10
Dipole Selection Rules and Photoexcitation Factor.....	13
Principles of Photoelectron Holography.....	21
Image Transform.....	29
Inversion of Constant-Initial-State Spectra.....	29
Full-Window Transform.....	34
Small-Cone Transform.....	37
3. EXPERIMENTAL PROCEDURES	41
System Setup	41
Electron Storage Ring.....	41
Monochromator System (Beamline).....	43
Vacuum Systems.....	44
Measurement Geometry.....	46
Sample Preparation	47
Data Acquisition	50
Data Acquisition System Setup.....	50
Data Acquisition Procedures.....	51
Data Analysis	55
EDC Peak Fitting.....	55
CIS Inversion and Image Transform.....	56

TABLE OF CONTENTS—Continued

	Page
4. EXPERIMENTAL RESULTS AND DISCUSSION.....	61
Si (100)-Se:1x1	61
Si (100)-Al:2x2	75
Si (100)-Mg:2x2	88
5. CONCLUSIONS AND COMMENTS.....	97
REFERENCES	99
APPENDIX.....	103
A complete set of 57 CIS's measured in the first quadrant of the emission hemisphere for Si(100)-Se:1x1.....	104

LIST OF TABLES

Table	Page
1. The atomic positions and image intensities of Si atoms of Si(100)-Se:1x1.....	65
2. Positions and image intensities of Si atoms for Si(100)-Al:2x2	78
3. Experimental results and theoretical calculations of the bond lengths for the Al ad-dimer and the underlying Si dimer.....	78
4. Positions and image intensities of Si atoms for Si(100)-Mg:2x2.....	89

LIST OF FIGURES

Figure	Page
1. Diagram of the process of photoelectron holography.....	2
2. Photoemission phenomenon.....	7
3. Schematic drawing of the Three-Step Model for the photoemission process.....	8
4. An energy-distribution curve (EDC) of a silicon substrate with zinc and selenium deposited on the surface.....	10
5. Coordinate systems and geometric relationship between the emitter and the scatterer.....	23
6. A schematic drawing for the full-window transform of a systems consisting two scatterers α and β	37
7. Schematic drawing of the choice of a small cone.....	38
8. Schematic drawing for the small-cone transform of a system consisting two scatterers α and β	40
9. Schematic layout of synchrotron radiation facility.....	42
10. Optical layout of the Ames/Montana extended-range grasshopper (ERG) and Seya-Namioka monochromator.....	43
11. Schematic layout (top view) of vacuum systems: Analysis Chamber, Intermediate Chamber, and Loadlock.....	45
12. Schematic drawing of sample's motion, HA-50's motion, and their geometric relationship.....	46
13. Schematic diagram of the connections among the monochromator, HA-50, and computer control system.....	50

LIST OF FIGURES—Continued

Figure	Page
14. EDC wide scan of ZnSe/Si taken at room temperature (photon energy 130 eV).....	51
15. A typical EDC curve of Se 3d taken at normal emission direction.....	52
16. A typical CIS spectrum of Se 3d taken at $\theta = 45^\circ$, $\phi = 50^\circ$ for Si(100)-Se:1x1.....	53
17. Schematic drawing of the distribution of the measured CIS positions in the first quadrant of the emission hemisphere.....	54
18. A CIS spectrum $I(k)$, and a non-diffractive reference curve $I_0(k)$ of Se 3d taken at $\theta = 45^\circ$, $\phi = 50^\circ$ for Si(100)-Se:1x1.....	56
19. The normalized diffraction curve $\chi(k)$ of Se 3d at $\theta = 45^\circ$, $\phi = 50^\circ$ for system Si(100)-Se:1x1.....	57
20. Si(100)-2x1 LEED pattern after 1100°C annealing.....	61
21. Diagram of the reconstructed Si(100) surface.....	62
22. X-Y horizontal planar cut of the image function at $Z = -1.1 \text{ \AA}$ for Si(100)-Se:1x1.....	66
23. X-Y horizontal planar cut of the image function at $Z = -2.4 \text{ \AA}$ for Si(100)-Se:1x1.....	67
24. X-Y horizontal planar cut of the image function at $Z = -3.7 \text{ \AA}$ for Si(100)-Se:1x1.....	68
25. X-Y horizontal planar cut of the image function at $Z = -5.1 \text{ \AA}$ for Si(100)-Se:1x1.....	69
26. X-Z vertical planar cut of the image function at $Y = 0$ for Si(100)-Se:1x1.....	70

LIST OF FIGURES—Continued

Figure	Page
27. Y-Z vertical planar cut of the image function at $X = 0$ for Si(100)-Se:1x1.....	71
28. 3-D diagram of Si(100)-Se:1x1 image results.....	72
29. Diagrams of biatomic-step single-domain Si(100)-2x1 surfaces and Se-adsorbed Si(100)-1x1 two-domain surfaces.....	73
30. Schematic drawing of the domain change process during the adsorption of Se on Si(100).....	74
31. Schematic drawing of (a) parallel and (b) orthogonal Al ad-dimer models.....	79
32. Si(100)-Al:2x2 LEED pattern at half of a monolayer coverage of Al.....	75
33. An X-Z vertical planar cut parallel to the step edges at $Y = 0$ for Si(100)-Al:2x2.....	80
34. An X-Y horizontal planar cut of the image function at $Z = -2.6 \text{ \AA}$ for Si(100)-Al:2x2.....	81
35. A line scan passing through intensity maximum positions C1 and C2 for Si(100)-Al:2x2.....	82
36. An X-Y horizontal planar cut of the image function at $Z = -1.2 \text{ \AA}$ for Si(100)-Al:2x2.....	83
37. A vertical planar cut through B1 and B4 for Si(100)-Al:2x2.....	84
38. Intensity contour plot of the vertical planar cut through B1 and B2 for Si(100)-Al:2x2.....	85
39. Local geometry of a parallel Al ad-dimer and corresponding holographic pattern.....	86

LIST OF FIGURES—Continued

Figure	Page
40. Local geometry of an orthogonal Al ad-dimer and corresponding holographic pattern.....	87
41. X-Y horizontal planar cut of the image function at $Z = -1.0 \text{ \AA}$ for Si(100)-Mg:2x2.....	91
42. Vertical planar cut of the image function through the diagonal plane contains A, D, and G silicon atoms for Si(100)-Mg:2x2.....	92
43. X-Y horizontal planar cut of the image function at $Z = -4.0 \text{ \AA}$ for Si(100)-Mg:2x2.....	93
44. X-Y horizontal planar cut of the image function at $Z = -2.4 \text{ \AA}$ for Si(100)-Mg:2x2.....	94
45. A 3-d schematic drawing of the local atomic structure of Si(100)-Mg:2x2 obtained from photoelectron holographic imaging results.....	95
46. Schematic drawing of the interfacial structures of Si(100)-Mg:2x2 obtained by photoelectron holographic imaging (PHI) and LEED results.....	96

ABSTRACT

It has always been one of the major goals in surface science to experimentally determine surface and interface structures. It has been demonstrated, in this thesis work, that three-dimensional images of the surface and interface structures can be obtained directly by means of photoelectron holography without any model calculations.

In the application of photoelectron holography to the study of the technologically important semiconductor interfaces, three systems have been chosen, Si(100)-Se:1x1, Si(100)-Al:2x2, and Si(100)-Mg:2x2. Of the three systems studied, selenium adsorbates are found to occupy the bridge sites. Selenium adsorbates have totally removed the reconstruction formed by surface silicon atoms, and the silicon surface is changed from single-domain to double-domain under the influence of selenium atoms, which implies that selenium atoms react with the silicon surface and etching occurs during the adsorption process. Aluminum on Si(100) has been a long-standing issue regarding the orientation of Al ad-dimers with respect to the underlying Si dimers. Photoelectron holographic imaging results of Si(100)-Al:2x2 clearly show that Al adsorbates form parallel ad-dimers. This is first time that photoelectron holographic imaging technique has been applied to a totally unexplored system, Si(100)-Mg:2x2. The image results successfully show that magnesium adsorbates occupy the four-fold hollow sites. In conjunction with LEED study, an interfacial structure is obtained.

CHAPTER 1

INTRODUCTION

It has always been one of the major goals in surface science to directly determine surface and interface structures. As the most recent development in the structural analysis field, a new photoelectron holography technique has demonstrated its unique power to obtain three-dimensional images of the surface and interface structures.

Photoelectron Holography and its Development

Photoelectron holography is a method of utilizing the wave characteristic of photoelectrons to produce photoelectron holograms which contain structural information of the atomic environment from which the photoelectrons are generated by photons.

The process of photoelectron holography is illustrated in Fig. 1. A photoelectron is ejected by a photon and the electron wave (reference wave) propagates outward. Part of the wave hits a neighboring atom (scatterer) and generates the scattered wave (object wave). Finally, the reference wave and object wave interfere and form an interference pattern (holographic pattern). The holographic pattern depends on the position of the scatterer. Therefore, information on the location of the scatterer is implicitly contained in the holographic pattern itself.

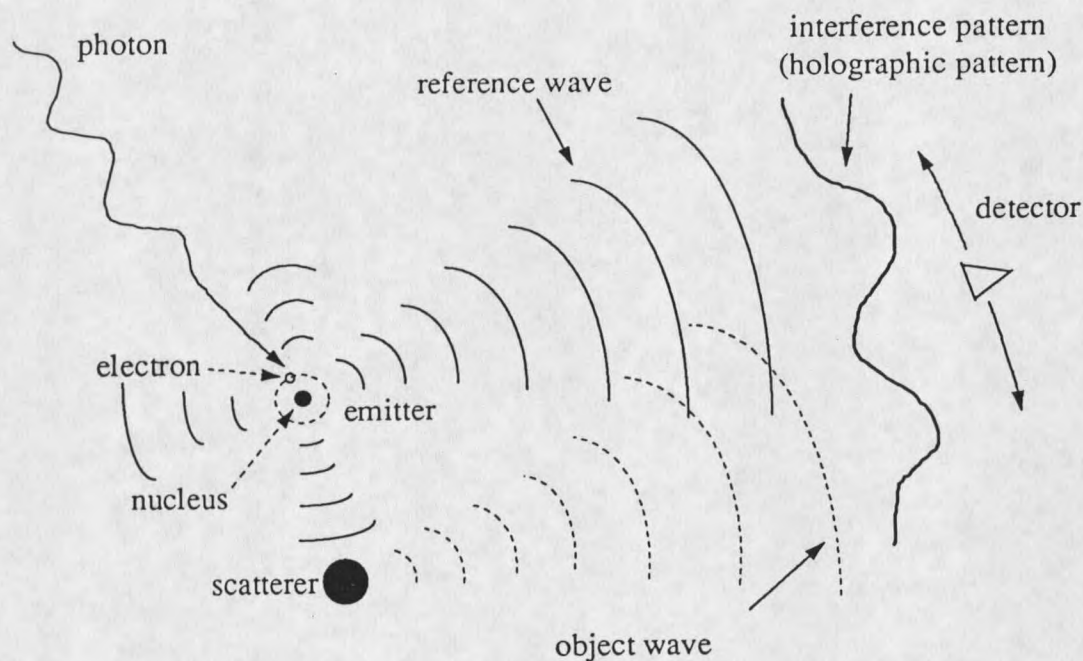


Fig. 1. Diagram of the process of photoelectron holography.

The conjecture by Szöke¹ that localized electron sources could produce three-dimensional holographic images of solids with atomic resolution has resulted in intense efforts to demonstrate this effect. In 1990, Harp *et al.*² reported the first experimental work on Cu (100) by single-energy photoelectron holography. Since then, many experiments have been performed with impressive results.^{3 4} In 1992, Tong *et al.*⁵ proposed an angle-resolved energy-dependent photoelectron holography method. The first experimental work based on this method was carried out by Wu *et al.*⁶ on the Al-adsorbed Si(111) $\sqrt{3} \times \sqrt{3}$ reconstructed surface with great success. In 1994, Wu *et al.*⁷ developed the small-cone method to improve the image quality and reduce the background noise.

This method has been proved to be an effective way to eliminate the artifacts and preserve the real atomic images.

Purposes and Motivations of the Present Work

Since photoelectron holography can elucidate the atomic structure of solids in three-dimensional view, its application to the study of semiconductor surfaces and interfacial structures has attracted researchers attention.

The Si (100) surface has been studied in great detail because of its technological importance. The structures formed by the interaction of a variety of foreign species with Si (100) have been under investigation for many years with various kinds of techniques. The interfacial structure is very important both theoretically and practically.

From a theoretical point of view, the interfacial structure parameters are very important for the calculation of electronic structure and also provide us a better understanding of the interaction between adsorbed elements and the silicon substrate.

From a practical point of view, silicon is heavily used as the substrate for growing a variety of compound semiconductor devices. The device quality depends on the growth quality, which in turn depends on the interfacial structure formed at the initial growth state. Therefore, the understanding of interfacial structure is essential for the growth of high quality crystals.

Finally, from a basic research point of view, the study of interfacial structures may lead to the discovery of novel structures and novel materials which will benefit the society in the future.

Despite the extensive studies of silicon interfacial structures, there are still many new and/or unsolved problems. For examples, the geometric orientation of Al ad-dimers, the adsorption site of Mg on silicon surfaces, and the formation of Se-Si interface are not well understood. Each of these structures has unique features of its own.

It is the purpose of this work to apply the photoelectron holographic imaging (PHI) technique to the experimental study of the interfacial structures formed by the adsorption of foreign elements on silicon surfaces to obtain detailed structural information on the adsorbate geometry.

The present work has accomplished the direct imaging of the atomic geometry of Si(100)-Se:1x1, Si(100)-Al:2x2, and Si(100)-Mg:2x2 systems with great success. Interfacial structures have been obtained with no ambiguity. The following section is a brief review of recent studies on the above mentioned systems.

Review of Previous Studies of Se, Al and Mg on Si (100) Surfaces

Se-adsorbed Si (100) surfaces have been studied both theoretically and experimentally. The theoretical work predicts that the Se atoms will occupy in the bridge sites.⁸ Experimental studies by photoemission core-level spectroscopy and low-energy electron diffraction (LEED) have reported a replacement of the (2x1) LEED pattern of the clean reconstructed Si(100) surface by a (1x1) pattern for a submonolayer film of Se on Si (100) after annealing to 550°C⁹. The results were interpreted as corresponding to the presence of 3/4 of a monolayer (ML)¹⁰ of Se atoms in the bridge sites. It has generally been accepted that Se adsorbates reside in the bridge sites; no image work has been done

so far either by photoelectron holographic imaging (PHI) or scanning tunneling microscopy (STM).

Al-adsorbed Si(100) surfaces have been investigated by several researchers by the methods of LEED, STM and low-energy electron diffraction intensity-voltage curves (LEED I-V).^{11 12 13 14 15 16} It has been demonstrated that a well-defined (2x2) phase forms at 0.5 monolayer coverage of Al atoms. It has been confirmed, both experimentally and theoretically, that Al adatoms form dimers on top of the Si surfaces, while preserving the underlying Si dimer configuration. The orientation of Al ad-dimers, with respect to the direction of the underlying Si dimer bonds, has been investigated extensively and has not yet come to an unambiguous conclusion. Some studies suggest the orthogonal ad-dimer structure,^{17 18} while others are consistent with the parallel ad-dimer configuration.^{19 20 21 22}

The interfacial structure of Mg on Si (100) had not been reported at the time when the studies reported in this thesis were carried out. In late 1994 a LEED and Auger study was published in which a 2x2 LEED pattern was observed after the deposition of Mg on Si(100) and subsequent annealing at 325°C.²³ A model, proposed on the basis of the observed LEED pattern, suggested that Mg atoms might occupy in the alternating four-fold hollow sites. No atomic image work has been reported so far.

Structure of the Paper

The rest of paper is divided into four chapters. In Chapter 2, the basic principles of photoemission are described. A detailed derivation of photoemission intensity is carried out. The principles of photoelectron holography and the image transform are presented

and discussed in thorough detail. Chapter 3 describes the experimental procedures including the system setup, sample preparation, data acquisition, and data analysis. In Chapter 4, three interfacial structures are presented based on the experimental imaging results. Chapter 5 is a summary of the present work.

CHAPTER 2

THEORY

Principles of PhotoemissionPhotoemission Phenomenon and the Three-Step Model

When a beam of light of sufficient photon energy impinges on a sample system (atom, molecule, or solid), electrons are emitted from the sample and can be detected (see Fig. 2). This is the photoemission phenomenon (or, photoelectric effect). The electrons ejected by the light are called photoelectrons.

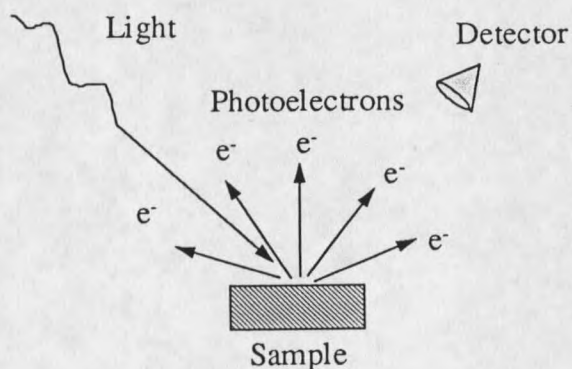


Fig. 2. Photoemission Phenomenon

In order for the photoemitted electrons to be detected, they must emerge from the interior of the sample into vacuum and proceed to the measuring device. This process is

usually discussed in terms of the three-step model.²⁴ These steps are: (1) optical excitation, (2) transport to the surface, and (3) escape into the vacuum (see Fig 3 below for emission from a core level).

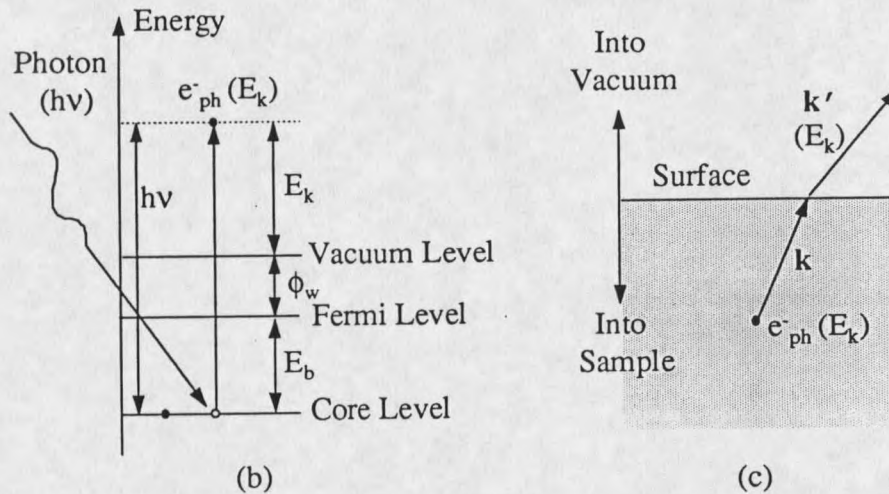


Fig. 3. Schematic drawing of the Three-Step Model for the photoemission process. (a) illustrates step one, and (b) depicts step two and three.

In Fig. 3(a), the first step of the model, a photon with energy $h\nu$ excites a core level electron with binding energy E_b to produce a photoelectron (labeled as e^-_{ph}) in a continuum state with kinetic energy E_k . The energy relationship can be written as

$$E_k = h\nu - E_b - \phi_w \quad (2.1)$$

where h is Planck's constant, ν is the photon frequency, and ϕ_w is the work function of the sample.

Figure 3(b) depicts that the photoelectron is transported to the surface, and then escapes into the vacuum, corresponding to steps two and three, respectively. Because of

the potential barrier at the surface, the photoelectron momentum (*i.e.* the wave vector) will change from \mathbf{k} to \mathbf{k}' . These vectors have following relationship:

$$k_{\parallel} = k'_{\parallel}, \quad (2.2a)$$

$$k_{\perp}^2 = k'_{\perp}{}^2 + (2m_e V) / \hbar^2, \quad (2.2b)$$

where k_{\parallel} and k'_{\parallel} are the components of \mathbf{k} and \mathbf{k}' parallel to the surface, k_{\perp} and k'_{\perp} are the components of \mathbf{k} and \mathbf{k}' perpendicular to the surface, m_e is the electron mass, $\hbar = h/2\pi$, and V is the surface potential barrier (also called the innerpotential). Equation (2.2a) states that the photoelectron momentum is conserved parallel to the surface, but not in the direction perpendicular to the surface. Equation (2.2b) is derived from the conservation of energy condition

$$\hbar^2 k^2 / 2m_e = \hbar^2 k'^2 / 2m_e + V, \quad (2.3)$$

along with the conditions $k^2 = k_{\parallel}^2 + k_{\perp}^2$, and $k'^2 = k'_{\parallel}{}^2 + k'_{\perp}{}^2$.

The atoms in the sample contain many kinds of core-level electrons; as long as Eq. (2.1) holds, those electrons can be excited to become photoelectrons. If a detector is placed at a direction $\hat{\mathbf{k}}'$, one can record the photoelectron signal intensity vs. kinetic energy to obtain an energy-distribution curve (EDC). Figure 4 displays a typical EDC taken from the silicon substrate with zinc and selenium deposited on the surface. The photon energy is 130 eV. The horizontal axis is the kinetic energy of the photoelectron, and the vertical axis is the intensity of the photoelectron. The atomic label (Si 2p, Se 3d, and Zn 3d) represents the photoelectron initial state. The Si Auger peak is due to the emission of silicon LMM Auger electrons, which will not be dealt with in this work.

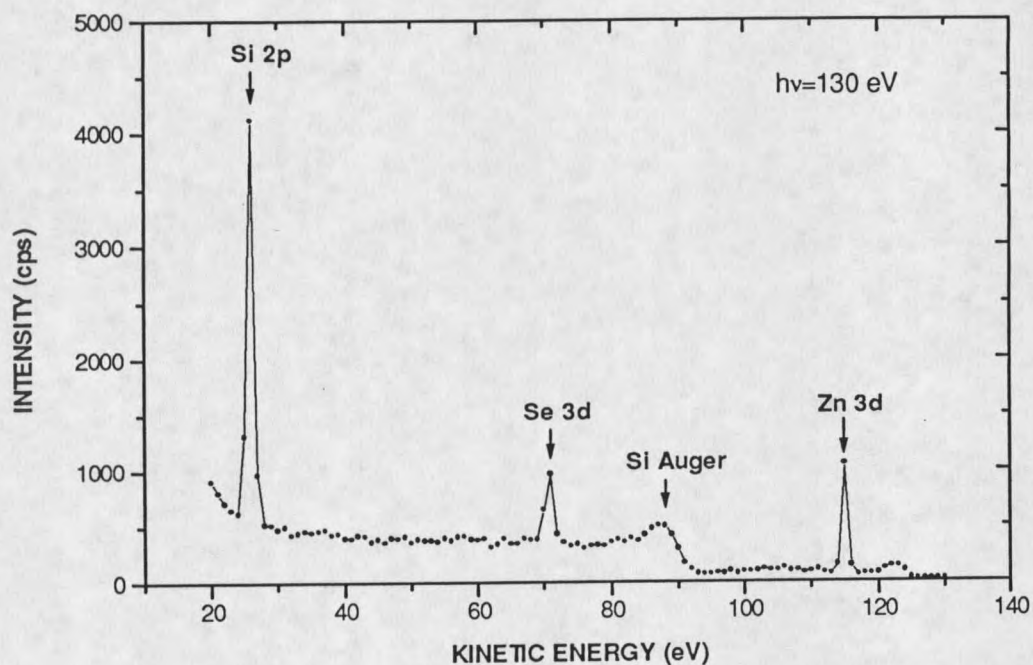


Fig. 4. An energy-distribution curve (EDC) of a silicon substrate with zinc and selenium deposited on the surface.

Quantum Mechanical Description of the Photoemission Process

Single-Atom System

In the case of one electron in an isolated atom, the Hamiltonian of the system can be written as

$$H_0 = \mathbf{p}^2 / 2m_e + V(\mathbf{r}) \quad (2.4)$$

where \mathbf{p} ($=-i\hbar\nabla$, and $\nabla\equiv\hat{x}\frac{\partial}{\partial x} + \hat{y}\frac{\partial}{\partial y} + \hat{z}\frac{\partial}{\partial z}$) is the momentum operator, $V(\mathbf{r})$ is the atomic potential, and \mathbf{r} is the position vector. In the case of a central potential, the potential is angle-independent, *i.e.* $V(\mathbf{r}) = V(r)$ where $r=|\mathbf{r}|$.

Before we move on, we need to set up our coordinate system. It is convenient to use spherical coordinates in the following discussion. The coordinate system is defined as follows: the origin is at the atomic center, the polar angle θ is the angle between position vector \mathbf{r} and the z axis, and the azimuthal angle ϕ is the angle between the projection of \mathbf{r} on the x - y plane and the x axis.

The time-independent Schrödinger equation is

$$H_0\Psi = E\Psi \quad (2.5)$$

It is assumed that the wave function Ψ can be separated into the product of an angle-dependent wave function and a radial wave function by the method of separation of variables as follows

$$\Psi = R(r) \Theta(\theta, \phi) \quad (2.6)$$

where $R(r)$ is the radial wave function, and $\Theta(\theta, \phi)$ is the angular wave function, which for a central force satisfy the following equations

$$-\left[\frac{1}{\sin\theta} \frac{\partial}{\partial\theta} \left(\sin\theta \frac{\partial}{\partial\theta} \right) + \frac{1}{\sin^2\theta} \frac{\partial^2}{\partial\phi^2} \right] \Theta(\theta, \phi) = l(l+1) \Theta(\theta, \phi) \quad (2.7a)$$

and

$$-\frac{\hbar^2}{2m_e} \left[\frac{1}{r^2} \frac{\partial}{\partial r} \left(r^2 \frac{\partial}{\partial r} \right) + \frac{l(l+1)\hbar^2}{2m_e r^2} + V(r) \right] R(r) = E R(r) \quad (2.7b)$$

where Eqs. (2.7a) and (2.7b) are called the angular equation and the radial equation, respectively.

The solutions of the angular equation (2.7a) are the spherical harmonics $Y_{lm}(\theta, \phi)$, with (l, m) being the angular momentum quantum number and magnetic quantum number, respectively.

The solutions for the radial equation (2.7b) fall into two parts: (a) for $E < 0$, Equation (2.7b) has discrete eigenvalues E_n with n (the principal quantum number) being one of the positive integers 1, 2, 3, The corresponding eigenfunctions are written as $R_{nl}(r)$. (b) for $E > 0$, the electron is in a continuum state, *i.e.* $E (=E_k$, the electron's kinetic energy) is a continuous variable. The corresponding radial wave function is denoted as $R_{kl}(r)$, where the index k also varies continuously and is normally taken to be the electron wave number. The asymptotic behavior of the radial function $R_{kl}(r)$ is that of a spherical wave, as can be seen from the following discussion.

Let us first make the substitution

$$R(r) = u(r) / r. \quad (2.8)$$

Then Eq. (2.7b) can be rewritten as

$$-\frac{\hbar^2}{2m_e} \frac{d^2 u}{dr^2} + \left[V(r) + \frac{l(l+1)\hbar^2}{2m_e r^2} \right] u = E u \quad (2.9)$$

When $r \rightarrow \infty$, $V(r) \rightarrow 0$. In this limit Eq. (2.9) may be written as

$$\frac{d^2 u}{dr^2} + k^2 u = 0 \quad (2.10)$$

where $k^2 = 2m_e E_k / \hbar^2$, and k is usually referred as electron wave number. We can easily see that

$$u \xrightarrow{r \rightarrow \infty} e^{\pm ikr} \quad (2.11)$$

Using Eq. (2.8), we have

$$R(r) = R_{kl}(r) \xrightarrow{r \rightarrow \infty} \frac{e^{\pm ikr}}{r} \quad (2.12)$$

where the plus sign represents the outgoing wave, and the minus sign represents the incoming wave.

The eigenfunctions for the system are given as follows:

$$\Phi_{nlm}(r, \theta, \phi) = R_{nl}(r) Y_{lm}(\theta, \phi) \quad (2.13a)$$

$$\Phi_{klm}(r, \theta, \phi) = R_{kl}(r) Y_{lm}(\theta, \phi). \quad (2.13b)$$

Equations (2.13a) and (2.13b) are the eigenfunctions for bound states and continuum states, respectively.

Dipole Selection Rules and the Photoexcitation Factor

Before the transition, the electron occupies an initial state $|i\rangle$, denoted as $|n_0 l_0 m_0\rangle$.

The initial state wave function Φ_i is

$$\Phi_i(r, \theta, \phi) = R_{n_0 l_0}(r) Y_{l_0 m_0}(\theta, \phi) \quad (2.14)$$

where n_0 is the principle quantum number, l_0 is the angular momentum number, and m_0 is the magnetic momentum number, of the initial state.

The photoemission process starts with the absorption of a photon by an atom and subsequent emission of the photoelectron. This process can be described by the interaction

of a core-level electron with the external electromagnetic field. Suppose we have a monochromatic photon of energy $h\nu$ incident on an atom. The electric field of the photon is given as

$$\mathbf{E}(\mathbf{r}, t) = \hat{\mathbf{e}} E_0 e^{i(\mathbf{k}_\omega \cdot \mathbf{r} - \omega t)}. \quad (2.15)$$

Where $\hat{\mathbf{e}}$ is the polarization vector, taken to be along the z axis, E_0 is the amplitude of the electric field, \mathbf{k}_ω is the photon wave vector, \mathbf{r} is the position vector measured from the center of the atom, and ω is the photon's angular frequency ($\omega = 2\pi\nu$).

In practice, in the type of experiments described here, the photon energy $h\nu$ is in the range from 100 eV to 240 eV, which corresponds to a photon wavelength (λ_ω) 120 Å to 50 Å, respectively. Then $k_\omega r \equiv a_0 / \lambda_\omega \ll 1$ holds, *i.e.* the wavelength is much larger than the atomic size. Thus, we can ignore the space dependence in the external field and Eq. (2.15) can be simplified as

$$\mathbf{E}(\mathbf{r}, t) = \hat{\mathbf{e}} E_0 e^{-i\omega t}. \quad (2.16)$$

Since the photon wavelength is much larger than the atom size, we can use the dipole approximation to describe the interaction between the atom and the electromagnetic field. With this approximation, the interaction Hamiltonian can be written as

$$H' = -e \mathbf{r} \cdot \mathbf{E}(\mathbf{r}, t) = -e \mathbf{r} \cdot \hat{\mathbf{e}} E_0 e^{i\omega t} = -e E_0 r \cos\theta e^{i\omega t} \quad (2.17)$$

where e is electron charge, and θ is the angle between the position vector \mathbf{r} and the polarization vector $\hat{\mathbf{e}}$ (*i.e.* the z axis). The total Hamiltonian of the system in the presence of external field is as follows:

$$H = H_0 + H' \quad (2.18)$$

where H_0 is the unperturbed Hamiltonian in the form of Eq. (2.4).

Let Ψ be the wave function in the presence of external field. It must satisfy the time-dependent Schrödinger equation

$$i\hbar \frac{\partial}{\partial t} \Psi = H \Psi. \quad (2.19)$$

We can expand Ψ in terms of the eigenstates $\{|j\rangle\}$ of H_0 as follows:

$$\Psi = \sum_j C_j |j\rangle, \quad (2.20)$$

where C_j are coefficients that must be determined, and the summation includes both the bound states and continuum states. Then, substituting Eq. (2.20) into Eq. (2.19), we have

$$i\hbar \frac{\partial}{\partial t} \sum_j C_j |j\rangle = (H_0 + H') \sum_j C_j |j\rangle. \quad (2.21)$$

For a state $|f\rangle \in \{|j\rangle\}$, we apply $\langle f|$ to the left side and use the orthogonality of the eigenstates to obtain the following result

$$i\hbar \frac{\partial}{\partial t} C_j \delta_{fj} = \sum_j E_j C_j \delta_{fj} + \sum_j C_j \langle f|H'|j\rangle \quad (2.22)$$

where δ_{ij} is the Kronecker delta defined as

$$\delta_{fj} = \begin{cases} =1 & (f=j) \\ =0 & (f \neq j) \end{cases} \quad (2.23)$$

Thus, Eq. (2.22) becomes

$$i\hbar \frac{\partial}{\partial t} C_f = E_f C_f + \sum_j C_j H'_{fj} \quad (2.24)$$

where E_f is the energy of the eigenstate $|f\rangle$, and H'_{fj} is defined as

$$H'_{fj} = \langle f|H'|j\rangle = \langle n \ l \ m | H' | n' \ l' \ m' \rangle \quad (2.25a)$$

or

$$H'_{fj} = N \int R_{n'l}(r) Y_{lm}^*(\theta, \phi) H'(r, \theta, \phi) R_{n'l}(r) Y_{l'm'}(\theta, \phi) r^2 dr d\Omega \quad (2.25b)$$

where N is the normalization factor, $d\Omega = \sin\theta d\theta d\phi$, (n, l, m) are the quantum numbers for state $|f\rangle$ (or $\langle f|$), (n', l', m') are the quantum numbers of state $|j\rangle$, and the integration is over all space. Then we make the substitution

$$C_f = B_f e^{iE_f t/\hbar}, \quad (2.26)$$

and Eq. (2.24) becomes

$$i\hbar \frac{\partial}{\partial t} B_f = \sum_j e^{i\omega_{fj} t} H'_{fj} B_j \quad (2.27)$$

where

$$\omega_{fj} = (E_f - E_j)/\hbar. \quad (2.28)$$

We now expand B_j as follows:

$$B_f = B_f^{(0)} + B_f^{(1)} + B_f^{(2)} + \dots \quad (2.29)$$

where $B_f^{(0)}, B_f^{(1)}, B_f^{(2)}, \dots$ signify expansion coefficients of zeroth order, first order, second order, and so on in the strength of the external potential.

We have assumed in the beginning of the section that the system is initially in the state $|i\rangle$, i.e. $B_f(t=0) = \delta_{fi}$, applying first-order perturbation theory to Eq. (2.27) we obtain

$$B_f = \delta_{fi} + \frac{1}{i\hbar} \int_0^t e^{i\omega_{fi} t'} H'_{fi} dt'. \quad (2.30)$$

Usually we consider transitions between two different states, i.e. $|f\rangle \neq |i\rangle$. Thus, Eq. (2.30) becomes

$$B_f = \frac{1}{i\hbar} \int_0^t e^{i\omega_{fi} t'} H'_{fi} dt'. \quad (2.31)$$

The transition is determined by H'_{fi} . In the dipole approximation, and when the external field is of the form of a plane wave as in Eq. (2.16), H'_{fi} can be written as (cf. Eq. (2.25a))

$$H'_{fi} = \langle n_0 l_0 m_0 | e E_0 r \cos \theta e^{-i \omega t} | n l m \rangle \quad (2.32a)$$

or

$$H'_{fi} = N e E_0 e^{-i \omega t} \langle l_0 m_0 | \cos \theta | l m \rangle \int R_{n_0 l_0}(r) R_{nl}(r) r^3 dr \quad (2.32b)$$

By examination of the angular integral in Eq. (2.32b),

$$\begin{aligned} \langle l_0 m_0 | \cos \theta | l m \rangle &= \int Y_{l_0 m_0}^*(\theta, \phi) \cos \theta Y_{lm}(\theta, \phi) d\Omega \\ &= \int [a Y_{l_0+1, m_0}^*(\theta, \phi) + b Y_{l_0-1, m_0}^*(\theta, \phi)] Y_{lm}(\theta, \phi) d\Omega, \end{aligned} \quad (2.33)$$

where the integral is over all solid angles. By the orthogonality of spherical harmonics, we have

$$\langle l_0 m_0 | \cos \theta | l m \rangle = a \delta_{l_0+1, l} \delta_{m_0 m} + b \delta_{l_0-1, l} \delta_{m_0 m} \quad (2.34)$$

where

$$a = \sqrt{\frac{(l_0+1)^2 - m_0^2}{(2l_0+1)(2l_0+3)}}, \quad b = \sqrt{\frac{(l_0+m_0+1)(l_0+m_0+2)}{(2l_0+1)(2l_0+3)}}. \quad (2.35)$$

We can easily see in (2.34), in order to have non-vanishing transition, the following conditions have to be met:

$$l = l_0 \pm 1, \quad (2.36a)$$

and

$$m = m_0. \quad (2.36b)$$

Equations (2.36a) and (2.36b) are often called the *dipole transition selection rules*.

Rewriting Eq. (2.32b) as

$$H'_{fi} = H'_{fi} e^{-i \omega t} \quad (2.37)$$

where

$$H'_{fi} = N e E_0 \langle l_0 m_0 | \cos \theta | l m \rangle \int R_{n_0 l_0}(r) R_{nl}(r) r^3 dr \quad (2.38a)$$

or

$$H'_{fi} = N e E_0 (a \delta_{l_0+1,l} + b \delta_{l_0-1,l}) \delta_{m_0 m} \int R_{n_0 l_0}(r) R_{nl}(r) r^3 dr \quad (2.38b)$$

H'_{fi} , which is called the transition matrix element, governs the transition process.

Substituting Eq. (2.37) into Eq. (2.31), we have

$$B_f = H'_{fi} \frac{1}{\hbar} \frac{e^{-i(\omega - \omega_{fi})t} - 1}{\omega - \omega_{fi}} \quad (2.39)$$

When the time t is long enough, we have

$$B_f = H'_{fi} \frac{2\pi i}{\hbar} e^{-i(\omega - \omega_{fi})t/2} \delta(\omega - \omega_{fi}) \quad (2.40)$$

where we have used the following relationship:

$$\lim_{t \rightarrow \infty} \frac{\sin((\omega - \omega_{fi})t/2)}{(\omega - \omega_{fi})/2} = 2\pi \delta(\omega - \omega_{fi}) \quad (2.41)$$

where $\delta(\omega - \omega_{fi})$ is the Dirac δ function, which has the following characteristics:

$$\delta(\omega - \omega_{fi}) = \begin{cases} 0 & (\omega \neq \omega_{fi}) \\ \infty & (\omega = \omega_{fi}) \end{cases} \quad (2.42a)$$

$$\int_{-\infty}^{\infty} \delta(\omega - \omega_{fi}) d\omega = 1 \quad (2.42b)$$

The meaning of the δ function is straightforward. In order to have a substantial transition, the condition $\omega = \omega_{fi}$ must be satisfied, *i.e.*

$$\hbar\omega = \hbar\omega_{fi} \quad (2.43a)$$

or

$$\hbar\omega = E_f - E_i \quad (2.43b)$$

which is the energy conservation law. This means that transition from initial state $|i\rangle$ to a possible excited state $|f\rangle$ has to satisfy the condition of conservation of energy. Substituting Eq. (2.40) into Eq. (2.26), and the latter into Eq. (2.20), we obtain the final state after the transition

$$\Psi = \sum_f H'_{fi} \frac{2\pi i}{\hbar} e^{-iE_f t/\hbar} e^{-i(\omega - \omega_{fi})t/2} \delta(\omega - \omega_{fi}) |f\rangle \quad (2.44)$$

where the index f represents the (n, l, m) indices. Explicitly, the summation over f is equivalent to the sum over n, l , and m , *i.e.*

$$\sum_f = \sum_n \sum_{lm} \quad (2.45)$$

Usually the possible excited states are not within the range of bound states, but are in the continuum. Then summation over the index n in the continuum states can be replaced by an integration, *i.e.*

$$\sum_n \rightarrow \int \rho(E) dE \quad (2.46)$$

where $\rho(E)$ is the density of states, which has the form

$$\rho(E) = (4\pi m_e / \hbar^2) k \quad (2.47)$$

for free electrons, and k is photoelectron wave number given as follows:

$$k = (2m_e E_k / \hbar^2)^{1/2} \quad (2.48)$$

where E_k is the photoelectron kinetic energy.

With the substitutions of Eqs. (2.45) and (2.46), Eq. (2.44) becomes

$$\Psi_k(\mathbf{r}, t) = e^{-iEk t/\hbar} \frac{8\pi^2 m_e}{\hbar^2} (ik) \sum_{lm} H_{ki} Y_{lm}(\theta, \phi) R_{kl}(r) \quad (2.49a)$$

or

$$\Psi_k(\mathbf{r}, t) = \Psi_k(\mathbf{r}) e^{-iEk t/\hbar} \quad (2.49b)$$

with

$$\Psi_k(\mathbf{r}) = \frac{8\pi^2 m_e}{\hbar^2} (ik) \sum_{lm} H_{ki} Y_{lm}(\theta, \phi) R_{kl}(r) \quad (2.50)$$

Equation (2.50) is the final state wave function of the photoelectron ejected from an initial core-level state $|i\rangle$. In the case $r \rightarrow \infty$, recalling Eq. (2.12), we can rewrite Eq. (2.50) as follows:

$$\Psi_k(\mathbf{r}) = F_k(\theta, \phi) \frac{e^{\pm ikr}}{r} \quad (\text{for } r \rightarrow \infty) \quad (2.51)$$

where

$$F_k(\theta, \phi) = \frac{8\pi^2 m_e}{\hbar^2} (ik) \sum_{lm} H_{ki} Y_{lm}(\theta, \phi) \quad (2.52)$$

which can be called the photoexcitation factor (analogous to the scattering factor).

In Eq. (2.51), the plus sign represents an outgoing radial wave and the minus sign represents an incoming radial wave. The choice of sign depends on the initial and boundary conditions of the physical system. In our work, the plus sign is selected because the photoelectron is emitted from the atom and propagates outwards.

Let us look at a simple case. Consider a core-level electron initially in an s state ($l_0=0, m_0=0$). According to the *dipole transition selection rule* Eqs. (2.36a) and (2.36b), we find the final state quantum numbers will be ($l = l_0 \pm 1 = \pm 1, m = m_0 = 0$). The angular

momentum quantum number cannot be negative, so the final state is ($l=1, m=0$), which is a p state. Then Eq. (2.52) becomes

$$F_k(\theta, \phi) = \frac{8\pi^2 m_e}{\hbar^2} (ik) H_{ki} Y_{10}(\theta, \phi) \quad (2.53)$$

Since

$$Y_{10}(\theta, \phi) = (3/4\pi)^{1/2} \cos\theta \quad (2.54)$$

we have

$$F_k(\theta, \phi) \propto \cos\theta \quad (2.55)$$

where θ is the polar angle with respect to photon's polarization direction. Equation (2.55) is well established for s -state excitation.

We have now obtained the photoelectron wave function Eq. (2.50). In the following section, we will discuss the photoelectron diffraction principle.

Principles of Photoelectron Holography

In the previous section, we obtained the photoelectron final state for a single-atom system in the presence of the external electromagnetic field. In this section we shall study the subsequent scattering of the ejected photoelectron by the neighboring atoms in the case of a solid system. In the environment of a solid, the photoelectron encounters "blocking" (neighboring atoms) in the sample unlike the case in a single-atom system where it does not encounter any blocking at all. When the photoelectron approaches these neighboring atoms, its path might be altered by scattering. In quantum mechanical

terms, the photoelectron wave will be scattered by the neighboring atoms. Photoelectron diffraction is the direct result of such scattering.

Using the result obtained from previous section, we write the photoelectron wave function as (*cf.* Eq. (2.50))

$$\Psi_k(\mathbf{r}) = \frac{8\pi^2 m_e}{\hbar^2} (ik) \sum_{lm} H_{ki} Y_{lm}(\theta, \phi) R_{kl}(r) \quad (2.56)$$

In the case $r \rightarrow \infty$, recalling Eq. (2.51), we have the asymptotic form for the photoelectron wave

$$\Psi_k(\mathbf{r}) = F_k(\theta, \phi) \frac{e^{ikr}}{r} \quad (2.57)$$

where $F_k(\theta, \phi)$ is the photoexcitation factor defined by Eq. (2.52). The outgoing wave is selected because the photoelectron is propagates outwards.

Usually we designate the atom from which the photoelectron is ejected as the emitter. The ejected photoelectron wave with no scattering is often called the emitted wave. The atoms neighboring the emitter are called scatterers. When the emitted wave (labeled as Ψ_{emi}) approaches the scatterers, it will be scattered, and the scattered waves (labeled as Ψ_{sca}) are generated. The final state wave function Ψ_f is the sum of the emitted wave and the scattered waves, *i.e.*

$$\Psi_f = \Psi_{\text{emi}} + \Psi_{\text{sca}} \quad (2.58)$$

with Ψ_f satisfying the Schrödinger equation

$$H \Psi_f = E_k \Psi_f \quad (2.59)$$

In Eq. (2.59), the Hamiltonian H is given as follows

$$H = -(\hbar^2/2m_e) \nabla'^2 + V_s(\mathbf{r}') \quad (2.60)$$

where $\nabla'^2 = (\partial^2/\partial x'^2 + \partial^2/\partial y'^2 + \partial^2/\partial z'^2)$ is the Laplacian operator, and $V_s(\mathbf{r}')$ the scattering potential in the scatterer coordinates $O'x'y'z'$. The coordinate systems and geometric relationship between the emitter and the scatterer are shown in Fig. 5.

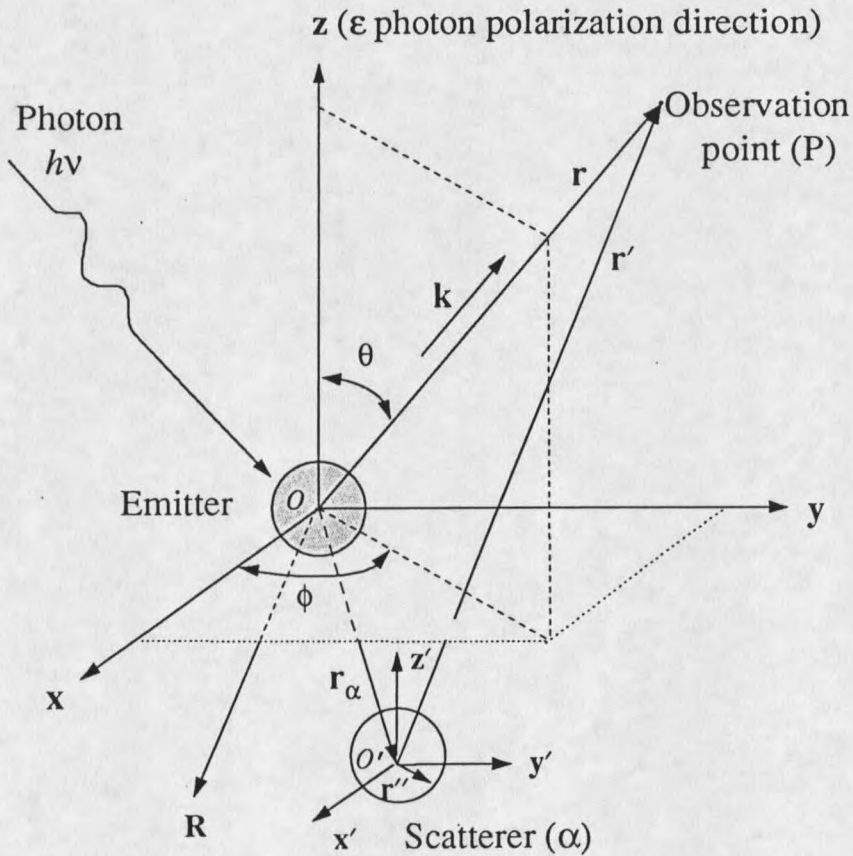


Fig. 5. Coordinate systems and geometric relationship between the emitter and the scatterer.

We shall use the convention that the z (or z') axis is along the polarization direction $\hat{\mathbf{e}}$ of the photon. In Fig. 5, there are two coordinate systems. The first one is set up at the emitter with its origin at the center of the emitter O . The second is set up at the

scatterer (α) with its origin at the center of the scatterer O' . The latter coordinate system is just a translation of the former by \mathbf{r}_α , the scatterer position vector measured from the center of the emitter. The scatterer is labeled with α , which will be used to index the scatterers in the following discussion. A vector variable \mathbf{R} measured from the center of the emitter is shown, which will also be used in the following discussion.

Employing the Green's function method in the scattering theory of quantum mechanics,²⁵ we obtain the final-state wave function Ψ_f , in the scatterer's coordinates

$$\Psi_f(\mathbf{r}') = \Psi_{\text{emi}}(\mathbf{r}') + \int d^3 r'' G_+(\mathbf{r}' - \mathbf{r}'') U_s(\mathbf{r}'') \Psi_f(\mathbf{r}'') \quad (2.61)$$

where

$$U_s(\mathbf{r}'') = (2m_0/\hbar^2) V_s(\mathbf{r}''). \quad (2.62)$$

Equation (2.61) is the integral scattering equation which has the final-state wave function on both side of the equation. The method of solving Eq. (2.61) is by iteration.

Making change of notation ($\mathbf{r}' \rightarrow \mathbf{r}''$, $\mathbf{r}'' \rightarrow \mathbf{r}'''$) in (2.61), we can write Eq. (2.61) as

$$\Psi_f(\mathbf{r}'') = \Psi_{\text{emi}}(\mathbf{r}''') + \int d^3 r''' G_+(\mathbf{r}'' - \mathbf{r}''') U_s(\mathbf{r}''') \Psi_f(\mathbf{r}'''). \quad (2.63)$$

Inserting (2.62) into (2.61), we obtain

$$\begin{aligned} \Psi_f(\mathbf{r}') = & \Psi_{\text{emi}}(\mathbf{r}') + \int d^3 r'' G_+(\mathbf{r}' - \mathbf{r}'') U_s(\mathbf{r}'') \Psi_{\text{emi}}(\mathbf{r}'') \\ & + \int d^3 r'' \int d^3 r''' G_+(\mathbf{r}' - \mathbf{r}'') U_s(\mathbf{r}'') G_+(\mathbf{r}'' - \mathbf{r}''') U_s(\mathbf{r}''') \Psi_f(\mathbf{r}'''). \end{aligned} \quad (2.64)$$

In order to solve Eq. (2.63), we will treat the scattering potential as a perturbation.

Employing the Born approximation to the first order, we obtain

$$\Psi_f(\mathbf{r}') = \Psi_{\text{emi}}(\mathbf{r}') + \int d^3 r'' G_+(\mathbf{r}' - \mathbf{r}'') U_s(\mathbf{r}'') \Psi_{\text{emi}}(\mathbf{r}''). \quad (2.65)$$

Recalling Eq. (2.58), we have

$$\Psi_{\text{sca}}^{\alpha}(\mathbf{r}') = \Psi_{\text{t}}(\mathbf{r}') - \Psi_{\text{emi}}(\mathbf{r}') = \int d^3 r'' G_{+}(\mathbf{r}' - \mathbf{r}'') U_{\text{s}}(\mathbf{r}'') \Psi_{\text{emi}}(\mathbf{r}'') . \quad (2.66)$$

In (2.65), $G_{+}(\mathbf{r}' - \mathbf{r}'')$ is the Green's function with the following form

$$G_{+}(\mathbf{r}' - \mathbf{r}'') = -\frac{1}{4\pi} \frac{e^{ik|\mathbf{r}' - \mathbf{r}''|}}{|\mathbf{r}' - \mathbf{r}''|} \quad (2.67)$$

which is a solution of the following inhomogeneous Helmholtz equation

$$(\nabla'^2 + k^2) G_{+}(\mathbf{r}' - \mathbf{r}'') = \delta(\mathbf{r}' - \mathbf{r}'') \quad (2.68)$$

For large r' , Eq. (2.66) can be expanded as

$$G_{+}(\mathbf{r}' - \mathbf{r}'') = -\frac{1}{4\pi} \frac{e^{ik|\mathbf{r}' - \mathbf{r}''|}}{|\mathbf{r}' - \mathbf{r}''|} \xrightarrow{r' \rightarrow \infty} -\frac{1}{4\pi} \frac{e^{ikr'}}{r'} e^{-i\mathbf{k}\cdot\mathbf{r}'} \quad (2.69)$$

In a solid (*e.g.* silicon substrate), the spacing between the nearest neighbors is about 2.4Å. The atomic interaction range is of the order of the Bohr radius a_0 (=0.529Å), which means the atomic interaction is well localized. In the first-order approximation in the radial wave expansion, the spherical wave is obtained. Recalling Eq. (2.57) and rewriting $\Psi_{\text{emi}}(\mathbf{r})$ in the scatterer's coordinates, we obtain

$$\Psi_{\text{emi}}(\mathbf{r}'') = F_k \left(\frac{\mathbf{r}_{\alpha} + \mathbf{r}''}{|\mathbf{r}_{\alpha} + \mathbf{r}''|} \right) \frac{e^{ik|\mathbf{r}' - \mathbf{r}''|}}{|\mathbf{r}' - \mathbf{r}''|} \quad (2.70)$$

where $\frac{\mathbf{r}_{\alpha} + \mathbf{r}''}{|\mathbf{r}_{\alpha} + \mathbf{r}''|}$ stands for the unit vector along $(\mathbf{r}_{\alpha} + \mathbf{r}'')$ direction. Since the atomic

interaction is well localized, the small-atom approximation²⁶ (*i.e.* r_{α} much larger than r'')

is used to expand Eq. (2.70). With the following approximations,

$$\frac{\mathbf{r}_{\alpha} + \mathbf{r}''}{|\mathbf{r}_{\alpha} + \mathbf{r}''|} \cong \frac{\mathbf{r}_{\alpha}}{|\mathbf{r}_{\alpha}|} = \hat{\mathbf{r}}_{\alpha} , \quad (2.71)$$

and

$$\frac{e^{ik|r' - r''|}}{|r' - r''|} \cong \frac{e^{ikr_\alpha}}{r_\alpha} e^{ik\hat{r}_\alpha \cdot r''}, \quad (2.72)$$

Eq. (2.70) becomes

$$\Psi_{\text{emi}}(\mathbf{r}'') = F_k(\hat{\mathbf{r}}_\alpha) \frac{e^{ikr_\alpha}}{r_\alpha} e^{ik\hat{r}_\alpha \cdot r''} \quad (2.73)$$

Substituting Eqs. (2.69) and (2.73) into Eq. (2.65), we obtain

$$\begin{aligned} \Psi_{\text{sca}}^\alpha(\mathbf{r}') &= -\frac{1}{4\pi} \int d^3r'' \frac{e^{ikr'}}{r'} e^{-i\mathbf{k} \cdot \mathbf{r}'} U_s(\mathbf{r}'') F_k(\hat{\mathbf{r}}_\alpha) \frac{e^{ikr_\alpha}}{r_\alpha} e^{ik\hat{r}_\alpha \cdot r''} \\ &= F_k(\hat{\mathbf{r}}_\alpha) \frac{e^{ikr_\alpha}}{r_\alpha} f_k(\hat{\mathbf{r}}_\alpha \cdot \hat{\mathbf{k}}) \frac{e^{ikr'}}{r'} \end{aligned} \quad (2.74)$$

where

$$f_k(\hat{\mathbf{r}}_\alpha \cdot \hat{\mathbf{k}}) = -\frac{1}{4\pi} \int d^3r'' e^{-i\mathbf{q} \cdot \mathbf{r}''} U_s(\mathbf{r}'') \quad (2.75)$$

is the scattering factor obtained by the Born approximation, where

$$\mathbf{q} = \mathbf{k} - \mathbf{k}_\alpha = \mathbf{k} - k\hat{\mathbf{r}}_\alpha \quad (2.76a)$$

and its modulus is

$$q = |\mathbf{q}| = 2k \sin(\hat{\mathbf{r}}_\alpha \cdot \hat{\mathbf{k}} / 2) \quad (2.76b)$$

From Fig. 3, we have

$$\mathbf{r}' = \mathbf{r} - \mathbf{r}_\alpha \quad (2.77)$$

When $r, r' \rightarrow \infty$, we obtain

$$r' = |\mathbf{r} - \mathbf{r}_\alpha| = r(1 - \hat{\mathbf{r}} \cdot \hat{\mathbf{r}}_\alpha) \quad (r, r' \rightarrow \infty) \quad (2.78)$$

Then rewriting Eq. (2.74) in the emitter coordinates Oxyz, we obtain the scattered wave as follows

$$\begin{aligned}
 \Psi_{\text{sca}}^{\alpha}(\mathbf{r}) &= f_k(\hat{\mathbf{r}}_{\alpha} \cdot \hat{\mathbf{k}}) \frac{e^{ikr}}{r} F_k(\hat{\mathbf{r}}_{\alpha}) \frac{e^{i(kr_{\alpha} - \mathbf{k} \cdot \mathbf{r}_{\alpha})}}{r_{\alpha}} \\
 &= \Psi_{\text{emi}}(\mathbf{r}) \left\{ f_k(\hat{\mathbf{r}}_{\alpha} \cdot \hat{\mathbf{k}}) \frac{F_k(\hat{\mathbf{r}}_{\alpha})}{F_k(\hat{\mathbf{k}})} \right\} \frac{e^{i(kr_{\alpha} - \mathbf{k} \cdot \mathbf{r}_{\alpha})}}{r_{\alpha}} \\
 &= \Psi_{\text{emi}}(\mathbf{r}) A_{\alpha}^k(\hat{\mathbf{k}}, \hat{\mathbf{r}}_{\alpha}) \frac{e^{i(kr_{\alpha} - \mathbf{k} \cdot \mathbf{r}_{\alpha})}}{r_{\alpha}} \tag{2.79}
 \end{aligned}$$

where $\Psi_{\text{emi}}(\mathbf{r})$ is the emitting wave given below (cf. Eq. (2.57))

$$\Psi_{\text{emi}}(\mathbf{r}) = F_k(\hat{\mathbf{k}}) \frac{e^{ikr}}{r}, \tag{2.80}$$

and

$$A_{\alpha}^k(\hat{\mathbf{k}}, \hat{\mathbf{r}}_{\alpha}) = f_k(\hat{\mathbf{r}}_{\alpha} \cdot \hat{\mathbf{k}}) \frac{F_k(\hat{\mathbf{r}}_{\alpha})}{F_k(\hat{\mathbf{k}})} \tag{2.81}$$

The final-state wave function of the photoelectron is the sum of the emitting wave and the total scattered wave. Since there is usually more than one scatterer that could contribute to the scattering process in a solid, the total scattered wave is the sum of the scattered waves generated by each scatterer. Considering this fact, the total scattered wave can be rewritten as follows

$$\Psi_{\text{sca}} = \Psi_{\text{sca}}^{\alpha} + \Psi_{\text{sca}}^{\beta} + \Psi_{\text{sca}}^{\gamma} + \dots \equiv \sum_{\alpha} \Psi_{\text{sca}}^{\alpha} \tag{2.82a}$$

$$= \Psi_{\text{emi}}(\mathbf{r}) \sum_{\alpha} A_{\alpha}^k(\hat{\mathbf{k}}, \hat{\mathbf{r}}_{\alpha}) \frac{e^{i(kr_{\alpha} - \mathbf{k} \cdot \mathbf{r}_{\alpha})}}{r_{\alpha}} \tag{2.82b}$$

where the summation is over all the scatterers ($\alpha, \beta, \gamma, \dots$). The symbol α has two meanings depending upon the context. When it appears in a context with no summation symbol, it means the label for scatterer α . When it appears in a context with the summation symbol over it, it then stands for the summation index being counted as $\alpha, \beta, \gamma, \dots$.

The photoelectron intensity $I(\hat{\mathbf{k}})$, measured at the observation point P (see Fig. 5) in the direction $\hat{\mathbf{k}}$, can be written as

$$I(\hat{\mathbf{k}}) = |\Psi_{\text{t}}|^2 = |\Psi_{\text{emi}} + \Psi_{\text{sca}}|^2, \quad (2.83a)$$

or

$$I(\hat{\mathbf{k}}) = I_0(\hat{\mathbf{k}}) + (\Psi_{\text{emi}}^* \Psi_{\text{sca}} + \Psi_{\text{emi}} \Psi_{\text{sca}}^*) + |\Psi_{\text{sca}}|^2 \quad (2.83b)$$

where

$$I_0(\hat{\mathbf{k}}) = |\Psi_{\text{emi}}|^2. \quad (2.84)$$

Let us examine Eq. (2.83b). The first term is the photoelectron's direct emitting wave intensity with no scattering. The middle terms inside the parenthesis are the cross-product terms involving the emitting waves and scattered waves. They are of the first order in the amplitude of the scattered waves. These cross terms reflect the interference between the emitting waves and scattered waves. As a result, an interference pattern (or diffraction pattern) is formed in space. The last term is of the second order in the amplitude of the scattered waves, and can be ignored.

A diffraction pattern, in principle, is the Fourier transform of some appropriate real-space density. It is the purpose of this work to extract out of this structural

information of the real space from the photoelectron diffraction data. A point to take account of is that the aforementioned diffraction pattern is immersed in the background signals coming from the direct emission of the photoelectrons.

In the laboratory, researchers always measure and record the total photoelectron intensity $I(\hat{\mathbf{k}})$. A way of separating the diffraction information from the background has to be established.

Let us define $\chi(\mathbf{k})$ as

$$\chi(\mathbf{k}) \equiv I(\hat{\mathbf{k}}) / I_0(\hat{\mathbf{k}}) - 1 \quad (2.85)$$

Substituting Eq. (2.83b) into Eq. (2.85), we obtain

$$\chi(\mathbf{k}) = [\Psi_{\text{emi}}^* \Psi_{\text{sca}} + \Psi_{\text{emi}} \Psi_{\text{sca}}^*] / I_0(\hat{\mathbf{k}}) \quad (2.86)$$

Substituting (2.82) into (2.86), we obtain

$$\chi(\mathbf{k}) = \sum_{\alpha} A_{\alpha}^k(\hat{\mathbf{k}}, \hat{\mathbf{r}}_{\alpha}) \frac{e^{i(k_{\alpha} - \mathbf{k} \cdot \mathbf{r}_{\alpha})}}{r_{\alpha}} + \sum_{\alpha} A_{\alpha}^{k*}(\hat{\mathbf{k}}, \hat{\mathbf{r}}_{\alpha}) \frac{e^{-i(k_{\alpha} - \mathbf{k} \cdot \mathbf{r}_{\alpha})}}{r_{\alpha}} \quad (2.87)$$

Equation (2.87) does not contain the direct emitting wave function of the photoelectron.

Extraction of diffraction data is thus achieved.

Image Transform

Inversion of Constant-Initial-State Spectra

A way of obtaining the photoelectron diffraction data is to first obtain the constant-initial-state spectrum (CIS).²⁷ In a CIS, photoelectron intensity is recorded at a fixed emission angle by keeping $(h\nu - E_i)$ constant while the photon energy $h\nu$ is varied in

a continuous fashion, where E_i is the energy of the initial state. In other words, a CIS is a plot of $I(k)$ (photoelectron intensity) vs. k (electron momentum) for a given initial-state electron at a fixed direction $\hat{\mathbf{k}}$. Such measurements require synchrotron radiation facilities which allow the photon energy to be changed continuously. Once the CIS's are obtained, they will be normalized by Eq. (2.85). The normalized CIS's, $\chi(\mathbf{k})$, are then inverted to yield the transform function $\Phi(\hat{\mathbf{k}}, \mathbf{R})$ as²⁸

$$\Phi(\hat{\mathbf{k}}, \mathbf{R}) = \int_{k_{\min}}^{k_{\max}} \chi(\hat{\mathbf{k}}, k) e^{-ikR} e^{ik \cdot \mathbf{R}} g(k) dk \quad (2.88)$$

where k_{\min} and k_{\max} are the minimum and maximum wave numbers of the CIS spectra, and $g(k)$ is a transform window function for reducing the noise near k_{\min} and k_{\max} . In our work, $g(k)$ is chosen to be the modified Hanning function which combines a flat region over the middle of the data range with a Hanning function at the ends,²⁹ that is:

$$g(k) = \begin{cases} \sin^2\left(\frac{\pi(k - k_{\min})}{2(k_2 - k_{\min})}\right) & \text{for } k_{\min} < k < k_2 \\ 1 & \text{for } k_2 < k < k_3 \\ \cos^2\left(\frac{\pi(k - k_3)}{2(k_{\max} - k_3)}\right) & \text{for } k_3 < k < k_{\max} \end{cases} \quad (2.89)$$

$$\text{with } k_2 = k_{\min} + b(k_{\max} - k_{\min})/2 \quad (2.90a)$$

$$k_3 = k_{\min} - b(k_{\max} - k_{\min})/2 \quad (2.90b)$$

where b is the "Hanning fraction": The relative range over which the Hanning function is acting. For $b=0$, there is no smooth effect; for $b=1$, a full Hanning function is used.²⁹

Now we define a path-length difference parameter ξ as

$$\xi \equiv R - \hat{\mathbf{k}} \cdot \mathbf{R} \quad (2.91)$$

where \mathbf{R} is a vector variable measured from the center of the emitter (see Fig. 5), and $R=|\mathbf{R}|$. Let δ be the angle between $\hat{\mathbf{k}}$ and \mathbf{R} , then Eq. (2.91) can be written as

$$\xi = R (1 - \cos\delta) \quad (2.92)$$

Since R is positive, and $|\cos\delta| \leq 1$, ξ is a non-negative parameter.

Substituting Eqs. (2.87) and (2.91) into Eq. (2.88), we obtain

$$\begin{aligned} \Phi(\hat{\mathbf{k}}, \mathbf{R}) = \int_{k_{\min}}^{k_{\max}} \left\{ \sum_{\alpha} A_{\alpha}^k(\hat{\mathbf{k}}) \frac{e^{i(kr_{\alpha} - \mathbf{k} \cdot \mathbf{r}_{\alpha})}}{r_{\alpha}} \right. \\ \left. + \sum_{\alpha} A_{\alpha}^{k*}(\hat{\mathbf{k}}) \frac{e^{-i(kr_{\alpha} - \mathbf{k} \cdot \mathbf{r}_{\alpha})}}{r_{\alpha}} \right\} e^{-ik\xi} g(k) dk \end{aligned} \quad (2.93)$$

$$\begin{aligned} \Phi(\hat{\mathbf{k}}, \mathbf{R}) = r_{\alpha}^{-1} \left\{ \sum_{\alpha} \int_{k_{\min}}^{k_{\max}} A_{\alpha}^k(\hat{\mathbf{k}}) e^{-ik[\xi - (r_{\alpha} - \hat{\mathbf{k}} \cdot \mathbf{r}_{\alpha})]} g(k) dk \right. \\ \left. + \sum_{\alpha} \int_{k_{\min}}^{k_{\max}} A_{\alpha}^{k*}(\hat{\mathbf{k}}) e^{-ik[\xi + (r_{\alpha} - \hat{\mathbf{k}} \cdot \mathbf{r}_{\alpha})]} g(k) dk \right\} \end{aligned} \quad (2.94)$$

Eq. (2.94) is a Fourier-like transform from momentum space to real space at the emission angle $\hat{\mathbf{k}}$. Eq. (2.94) will have a maximum when

$$\xi = \pm (r_{\alpha} - \hat{\mathbf{k}} \cdot \mathbf{r}_{\alpha}) \quad (2.95)$$

Since ξ is a non-negative parameter, and $(r_{\alpha} - \hat{\mathbf{k}} \cdot \mathbf{r}_{\alpha})$ is also non-negative, only the positive term is the acceptable solution. This means only the first integration term in Eq. (2.94) is the dominant one. Thus the twin-image term (the second integration term) is suppressed by this transform. Combining Eqs. (2.92) and (2.14), we obtain the maximum condition for Eq. (2.94)

$$R - \hat{\mathbf{k}} \cdot \mathbf{R} = r_{\alpha} - \hat{\mathbf{k}} \cdot \mathbf{r}_{\alpha} \quad (2.96)$$

The solutions of Eq. (2.96) are given as

$$R = r_\alpha \frac{1 - \hat{\mathbf{k}} \cdot \hat{\mathbf{r}}_\alpha}{1 - \hat{\mathbf{k}} \cdot \hat{\mathbf{R}}} \quad (2.97a)$$

or

$$R = \frac{C_\alpha^k}{(1 - \cos\delta)} \quad (2.97b)$$

with

$$C_\alpha^k = r_\alpha(1 - \hat{\mathbf{k}} \cdot \hat{\mathbf{r}}_\alpha) \quad (2.98)$$

being a non-negative constant determined by the emission angle $\hat{\mathbf{k}}$ and the scatterer position \mathbf{r}_α .

Equation (2.97a) (or (2.97b)) is the equation for a paraboloid with $\hat{\mathbf{k}}$ as its principal-axis direction and its vertex at $-(C_\alpha^k/2)\hat{\mathbf{k}}$. If we vary the emission angle $\hat{\mathbf{k}}$, we shall obtain a group of paraboloids. Let us examine the behavior of these paraboloids with different emission angle $\hat{\mathbf{k}}$. Selecting any one of these paraboloids, we can see that when vector variable \mathbf{R} is equal to \mathbf{r}_α , it satisfies Eq. (2.97a). This means that \mathbf{r}_α is on the surface of the selected paraboloid. Since the emission angle $\hat{\mathbf{k}}$ is not restricted, \mathbf{r}_α is on the surface of all these paraboloids. In other words, the scatterer position \mathbf{r}_α is intersected by all the paraboloids satisfying Eq. (2.97a).

We can prove that \mathbf{r}_α is the only position intersected by all these paraboloids, on the premise that Eq. (2.96) holds. To do this, assume there exists another position $\mathbf{r}_{\alpha'}$, which does not coincide with \mathbf{r}_α , *i.e.*

$$\mathbf{r}_{\alpha'} \neq \mathbf{r}_{\alpha}, \quad (2.99)$$

where $\mathbf{r}_{\alpha'}$ is intersected by all the paraboloids passing through \mathbf{r}_{α} . Then we have the following equation for position $\mathbf{r}_{\alpha'}$ (cf. Eq. (2.96))

$$R - \hat{\mathbf{k}} \cdot \mathbf{R} = r_{\alpha'} - \hat{\mathbf{k}} \cdot \mathbf{r}_{\alpha'} \quad (2.100)$$

Combining Eqs. (2.96) and (2.99), we obtain

$$r_{\alpha'} - \hat{\mathbf{k}} \cdot \mathbf{r}_{\alpha'} = r_{\alpha} - \hat{\mathbf{k}} \cdot \mathbf{r}_{\alpha} \quad (2.101a)$$

or

$$r_{\alpha'} - r_{\alpha} = \hat{\mathbf{k}} \cdot (\mathbf{r}_{\alpha'} - \mathbf{r}_{\alpha}) \quad (2.101b)$$

Making the following substitutions,

$$q' = r_{\alpha'} - r_{\alpha} \quad (2.102)$$

$$\mathbf{q} = \mathbf{r}_{\alpha'} - \mathbf{r}_{\alpha} \quad (2.103)$$

Eq. (2.101b) becomes

$$q' = \hat{\mathbf{k}} \cdot \mathbf{q} \quad (2.104)$$

Since $\mathbf{r}_{\alpha'}$ and \mathbf{r}_{α} are fixed, so are \mathbf{q} and q' . The following cases comprise all the possible values for q' :

case (I):

$$q' > 0 \quad (r_{\alpha'} > r_{\alpha}) \quad (2.105)$$

case (II):

$$q' = 0 \quad (|r_{\alpha'}| = |r_{\alpha}|, \hat{\mathbf{r}}_{\alpha'} \neq \hat{\mathbf{r}}_{\alpha}) \quad (2.106)$$

case (III):

$$q' < 0 \quad (r_{\alpha'} < r_{\alpha}) \quad (2.107)$$

Let ζ be the angle between \mathbf{k} and \mathbf{q} . The emission angle $\hat{\mathbf{k}}$ can be any direction in space. For $q' > 0$ (case I), we can choose $\zeta \geq 90^\circ$ such that $\hat{\mathbf{k}} \cdot \mathbf{q} < 0$, which violates the Eq. (2.104). This means $\mathbf{r}_{\alpha'}$ cannot be a vector different from \mathbf{r}_{α} . The same reasoning can be applied for cases (II) and (III): by choosing $\zeta \neq 90^\circ$, and $\zeta \leq 90^\circ$, Eq. (2.104) will not hold for case (II) and (III), respectively. Thus, we have proved that \mathbf{r}_{α} is the sole point intersected by all the paraboloids satisfying Eq. (2.96).

The complex amplitude of the paraboloid passing through scatterer α at a given emission angle $\hat{\mathbf{k}}$ can be written as

$$\Phi(\hat{\mathbf{k}}, \mathbf{r}_{\alpha}) \Big|_{R_k = C_{\alpha}^k / (1 - \cos \delta)} = r_{\alpha}^{-1} \int_{k_{\min}}^{k_{\max}} A_{\alpha}^k(\hat{\mathbf{k}}) g(k) dk \quad (2.108)$$

where a subscript $R_k = C_{\alpha}^k / (1 - \cos \delta)$ is used to distinguish the parabolic transform function $\Phi(\hat{\mathbf{k}}, \mathbf{r}_{\alpha})$ from the general transform function $\Phi(\hat{\mathbf{k}}, \mathbf{R})$.

Since all the paraboloids satisfying Eq. (2.96) pass through \mathbf{r}_{α} and each of them makes contribution to the intensity at this particular point, the intensity at position \mathbf{r}_{α} will be much higher than at other positions in space. By examining the intensity maxima of the transform function $\Phi(\hat{\mathbf{k}}, \mathbf{R})$ (cf. Eq. (2.94)), we can obtain the scatterer position relative to the emitter.

Full-Window Transform

An image function $U(\mathbf{R})$ is constructed by summing the transform function $\Phi(\hat{\mathbf{k}}, \mathbf{R})$ over all the emission angles, *i.e.*

$$U(\mathbf{R}) = \left| \sum_{\text{all } \hat{\mathbf{k}}} \Phi(\hat{\mathbf{k}}, \mathbf{R}) \right|^2 \quad (2.109)$$

Equation (2.109) is often referred to as the full-window transform and was first proposed by Tong *et al.*^{7,28}

Since the major contributions to Eq. (2.94) come from those paraboloids satisfying Eq. (2.97b), with the aid of Eq. (2.108), we can write Eq. (2.94) as

$$\Phi(\hat{\mathbf{k}}, \mathbf{R}) \equiv \sum_{\alpha} \Phi(\hat{\mathbf{k}}, \mathbf{r}_{\alpha}) \Big|_{R_{\hat{\mathbf{k}}} = C_{\alpha}^{\hat{\mathbf{k}}} / (1 - \cos \delta)} \quad (2.110)$$

which implies that the transform function $\Phi(\hat{\mathbf{k}}, \mathbf{R})$ can be viewed as the sum of the parabolic transform function $\Phi(\hat{\mathbf{k}}, \mathbf{r}_{\alpha})$ over all the scatterers. Substituting Eq. (2.110) into Eq. (2.109), we obtain

$$U(\mathbf{R}) = \left| \sum_{\text{all } \hat{\mathbf{k}}} \left\{ \sum_{\alpha} \Phi(\hat{\mathbf{k}}, \mathbf{r}_{\alpha}) \Big|_{R_{\hat{\mathbf{k}}} = C_{\alpha}^{\hat{\mathbf{k}}} / (1 - \cos \delta)} \right\} \right|^2 \quad (2.111)$$

Switching the summation order, we obtain

$$U(\mathbf{R}) = \left| \sum_{\alpha} \left\{ \sum_{\text{all } \hat{\mathbf{k}}} \Phi(\hat{\mathbf{k}}, \mathbf{r}_{\alpha}) \Big|_{R_{\hat{\mathbf{k}}} = C_{\alpha}^{\hat{\mathbf{k}}} / (1 - \cos \delta)} \right\} \right|^2 \quad (2.112)$$

We now define the scatterer transform function as

$$\Lambda(R_F(\mathbf{r}_{\alpha})) = \sum_{\text{all } \hat{\mathbf{k}}} \Phi(\hat{\mathbf{k}}, \mathbf{r}_{\alpha}) \Big|_{R_{\hat{\mathbf{k}}} = C_{\alpha}^{\hat{\mathbf{k}}} / (1 - \cos \delta)} \quad (2.113)$$

where $R_F(\mathbf{r}_{\alpha})$ stands for the group of paraboloids passing through \mathbf{r}_{α} for all the emission angles (*i.e.* a full-window summation). Then Eq. (2.112) can be written as

$$U(\mathbf{R}) = \left| \sum_{\alpha} \Lambda(R_F(\mathbf{r}_{\alpha})) \right|^2 \quad (2.114)$$

We rewrite the summation over scatterer index α in terms of each scatterer labeled as $\alpha, \beta, \gamma \dots$. Then Eq. (2.114) becomes

$$U(\mathbf{R}) = | \Lambda(R_F(\mathbf{r}_\alpha)) + \Lambda(R_F(\mathbf{r}_\beta)) + \Lambda(R_F(\mathbf{r}_\gamma)) + \dots |^2 \quad (2.115)$$

Expanding Eq. (2.115), we obtain the following expression:

$$U(\mathbf{R}) = | \Lambda(R_F(\mathbf{r}_\alpha)) |^2 + | \Lambda(R_F(\mathbf{r}_\beta)) |^2 + | \Lambda(R_F(\mathbf{r}_\gamma)) |^2 + \dots \\ + \sum_{\substack{\alpha, \beta \\ \alpha \neq \beta}} \{ \Lambda(R_F(\mathbf{r}_\alpha)) \Lambda^*(R_F(\mathbf{r}_\beta)) + \Lambda^*(R_F(\mathbf{r}_\alpha)) \Lambda(R_F(\mathbf{r}_\beta)) \} \quad (2.116)$$

In Eq. (2.116), the squared terms account for the individual transform for scatterers α, β, γ and so on. We will find the corresponding intensity maxima at positions $\mathbf{r}_\alpha, \mathbf{r}_\beta, \mathbf{r}_\gamma, \dots$, which correspond to the scatterer positions for scatterers $\alpha, \beta, \gamma, \dots$. From these maxima we can obtain the structural geometry relating the emitters (adsorbates) and the scatterers (substrate atoms). On other hand, a double summation term remains in Eq. (2.116) which accounts for the interference of different scatterer transform functions. This interference effect can sometimes build up notable intensity and produce substantial artifacts in the data beyond the scatterer intensity maxima. Figure 6 depicts the full-window transform of a system consisting of two scatterers α, β . Seven paraboloids passing through each scatterer, corresponding to seven emission angles, build up the intensity at each scatterer position. The paraboloids of scatterers α, β intersect each other and form artifacts.

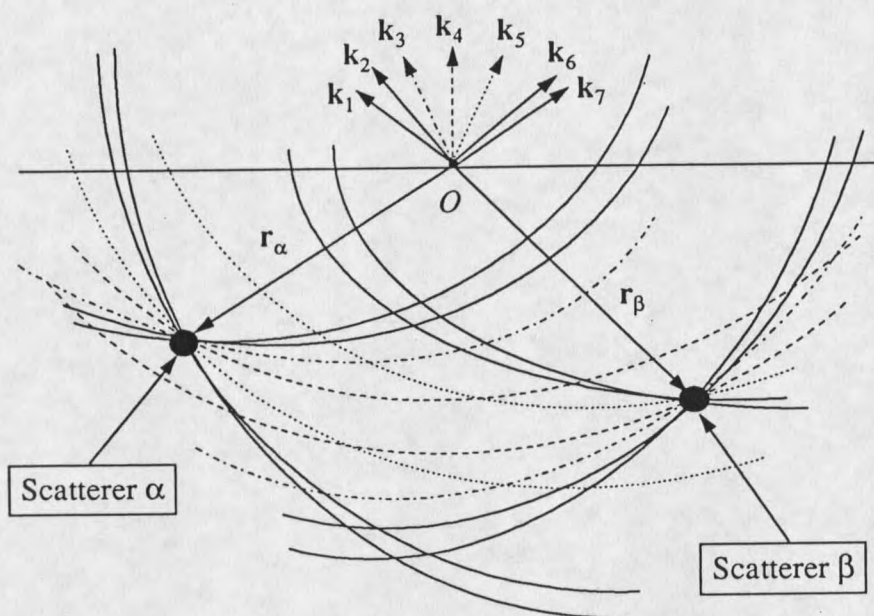


Fig. 6. A schematic drawing for the full-window transform of a system consisting two scatterers α and β . The emitter is at position O .

Small-Cone Transform

The small-cone method is introduced to reduce artifacts. In Eq. (2.109), if we sum the emission angles over a limited solid angle (*i.e.* a small cone) instead of all the emission angles, we can rewrite Eq. (2.109) as

$$U(\mathbf{R}) = \left| \sum_{\hat{\mathbf{k}} \in \text{Cone}(-\hat{\mathbf{R}}, w)} \Phi(\hat{\mathbf{k}}, \mathbf{R}) \right|^2 \quad (2.117)$$

In Eq. (2.117), the image function is constructed by summing the inverted CIS functions over a cone pointing in the $-\hat{\mathbf{R}}$ direction (vacuum side) with half-angle width w and vertex at the center of the emitter (see Fig. 7).

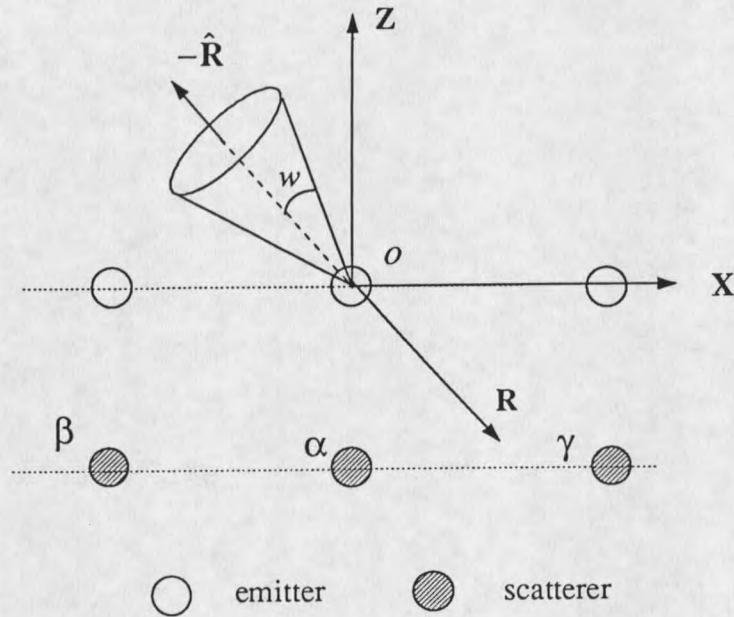


Fig. 7. Schematic drawing of the choice of a small cone.

The half-angle width w of the small cone can be easily obtained from experimental data by plotting a series of phases and amplitudes of $\Phi(\hat{\mathbf{k}}, \mathbf{R})$ vs. emission angle (usually polar angle or azimuthal angle). As demonstrated by Wu,⁷ the phase and amplitude of the inverted CIS function show slow variations in the neighborhood of the π scattering. Beyond that region, the phase changes rapidly.

Employing the result obtained in previous section (*cf.* Eq. (2.110)), we can write Eq. (2.117) as

$$U_{sc}(\mathbf{R}) = \left| \sum_{\hat{\mathbf{k}} \in \text{Cone}(-\hat{\mathbf{R}}, w)} \sum_{\alpha} \Phi(\hat{\mathbf{k}}, \mathbf{r}_{\alpha}) \Big|_{R_{\mathbf{k}} = C_{\alpha}^{\pm} / (1 - \cos \delta)} \right|^2 \quad (2.118)$$

or

$$U_{sc}(\mathbf{R}) = \left| \sum_{\alpha} \sum_{\hat{\mathbf{k}} \in \text{Cone}(-\hat{\mathbf{R}}, w)} \Phi(\hat{\mathbf{k}}, \mathbf{r}_{\alpha}) \Big|_{R_{\mathbf{k}} = C_{\alpha}^{\hat{\mathbf{k}}}/(1-\cos\delta)} \right|^2 \quad (2.119)$$

By analogy to Eq. (2.113), the definition of the scatterer transform function for the full window, we can write down the scatterer transform function for small cone as

$$\Lambda(R_S(\mathbf{r}_{\alpha})) = \sum_{\hat{\mathbf{k}} \in \text{Cone}(-\hat{\mathbf{R}}, w)} \Phi(\hat{\mathbf{k}}, \mathbf{r}_{\alpha}) \Big|_{R_{\mathbf{k}} = C_{\alpha}^{\hat{\mathbf{k}}}/(1-\cos\delta)} \quad (2.120)$$

where $R_S(\mathbf{r}_{\alpha})$ stands for the group of paraboloids passing through \mathbf{r}_{α} with emission angles within the small cone. Substituting Eq. (2.120) into Eq. (2.119), we obtain

$$U_{sc}(\mathbf{R}) = \left| \Lambda(R_S(\mathbf{r}_{\alpha})) + \Lambda(R_S(\mathbf{r}_{\beta})) + \Lambda(R_S(\mathbf{r}_{\gamma})) + \dots \right|^2 \quad (2.120)$$

or

$$U_{sc}(\mathbf{R}) = \left| \Lambda(R_S(\mathbf{r}_{\alpha})) \right|^2 + \left| \Lambda(R_S(\mathbf{r}_{\beta})) \right|^2 + \left| \Lambda(R_S(\mathbf{r}_{\gamma})) \right|^2 + \dots \\ + \sum_{\substack{\alpha, \beta \\ \alpha \neq \beta}} \{ \Lambda(R_S(\mathbf{r}_{\alpha})) \Lambda^*(R_S(\mathbf{r}_{\beta})) + \Lambda^*(R_S(\mathbf{r}_{\alpha})) \Lambda(R_S(\mathbf{r}_{\beta})) \} \quad (2.121)$$

The meaning of each term in (2.121) is the same as that of in (2.116) for the full-window transform, except that the emission angles are confined within the small cone.

The advantage of the small cone transform is fully discussed in reference 7. First, it optimally utilizes the experimental data to construct the parabolic transform function by including the in-phase paraboloids. Second, it reduces the interference of different scatterer transform functions. Since the paraboloids used in the transform are within the small cone, the number and intensity of the intersection between different scatterer transform functions are reduced compared to the full-window transform. Hence the image quality is improved. Figure 8 depicts the small-cone transform of a system consisting of

two scatterers α and β . Comparing Fig. 6 and Fig. 8, we can see that the intersection (artifacts) is reduced.

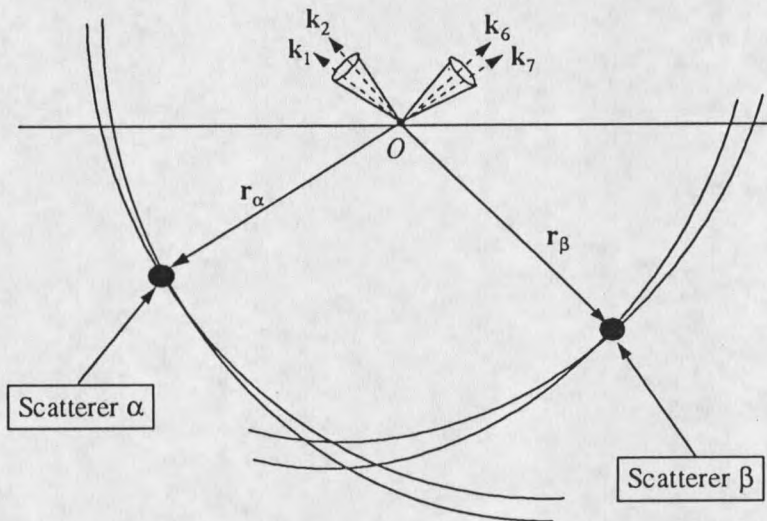


Fig. 8. Schematic drawing for the small-cone transform of a system consisting two scatterers α and β .

CHAPTER 3

EXPERIMENTAL PROCEDURES

System Setup

The experimental work was carried out at Synchrotron Radiation Center (SRC) of the University of Wisconsin-Madison, Stoughton, Wisconsin, on the 1 GeV storage ring. A series of bending magnets are placed along the ring to bend the electrons trajectory. When these electrons are bent, they radiate light. Then the light is introduced into a beamline system to obtain monochromatic light. An analysis chamber equipped with essential analytical devices is connected to the beamline. The above mentioned systems are all under ultra high vacuum (UHV) conditions. The sample is first introduced from the air to the loadlock, then to the intermediate chamber, and finally to the analysis chamber. This three-step sample transfer is to assure the UHV condition at the analysis chamber, which is a basic but crucial condition for keeping the cleanliness of the measured sample. A detailed description is given in the following sections.

Electron Storage Ring

The electron storage ring is essentially a long UHV pipe (about 89 meters in circumference) maintained by numerous UHV pumping units. The UHV condition is

essential for maintaining a relatively stable electron beam inside the ring. The electrons are ejected by the microtron at low energy (108 MeV) into the ring and then energized to 800 MeV (or 1 GeV). The electrons are ejected in bunches with a spatial separation about 5.93 meters (or a time separation 19.8 ns). Usually there are 15 bunches inside the ring at a time. A radio frequency (RF) cavity is placed inside the ring to maintain the electron energy. The RF frequency is 50.582 MHz. A series of bending magnets are placed along the ring to apply bending force to the fast moving (at nearly the speed of light) electrons to bend their trajectory and, most important, make the electrons radiate light, the so called synchrotron radiation. A schematic drawing of the synchrotron radiation facility is shown in Fig. 9.

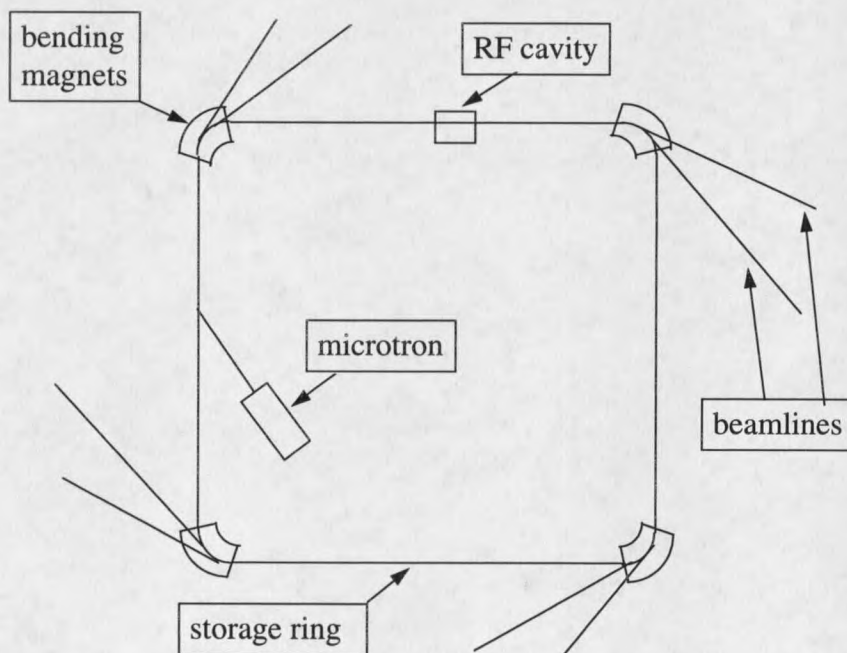


Fig. 9. Schematic layout of synchrotron radiation facility.

Monochromator System (Beamline)

The radiation light is composed of a wide band of photon frequencies. In order to use a certain frequency light, a monochromator system is built up for such purpose. A monochromator system is often referred to as a beamline. The beamline on which this work was carried out is the Ames/Montana beamline. The beamline is designed by Dr. C. Olson of Iowa State University. The optical layout is shown in Fig. 10 below.

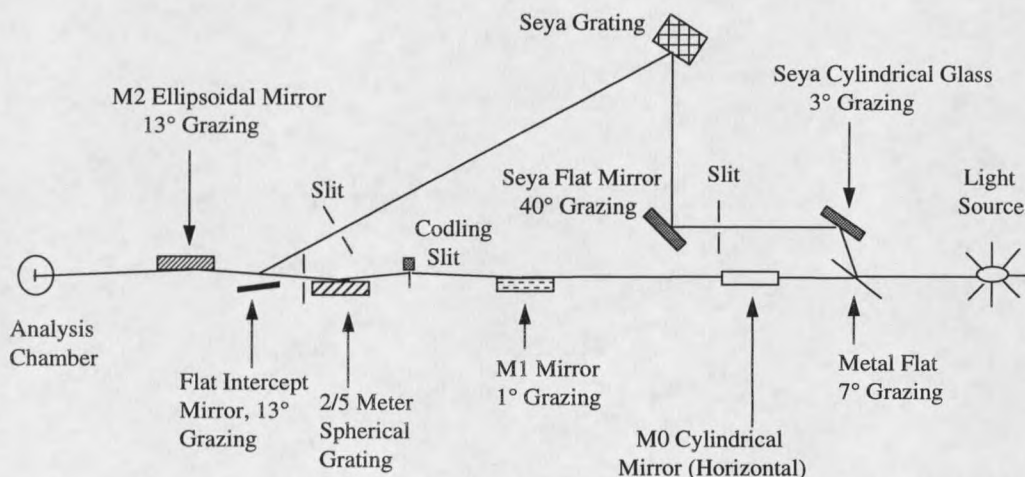


Fig. 10. Optical layout of the Ames/Montana extended-rang grasshopper (ERG) and Seya-Namioka monochromator.³⁰

The Ames/Montana Monochromator has several gratings for selecting different photon energy ranges. Two meter ERG (extended-rang grasshopper) covers from 40 eV to 240 eV, five meter ERG from 300 eV to 1200 eV. The Seya-Namioka monochromator has four gratings covering 6 eV to 50 eV. The ERG is mainly used for core level electron measurements and Seya for valence band studies. The photoelectron diffraction work utilizes the two-meter ERG.

Vacuum Systems

The vacuum system setup has three stages (see Fig. 11). The first stage is the loadlock. It can be easily vented to air and then pumped down to 1×10^{-5} torr in 10 min by a turbo-mechanical pump-stand. The second stage is the intermediate chamber, which isolates with the first stage (loadlock) by a gate valve. Its base pressure is 5×10^{-10} torr. The third stage is the analysis chamber where base pressure is $5-7 \times 10^{-11}$ torr. A gate valve is used to isolate the analysis chamber from the intermediate chamber. The three-stage setup is designed for fast sample transfer without breaking the UHV condition in the analysis chamber and the intermediate chamber. The first stage (loadlock) is used for loading the sample from the air. The intermediate chamber is used for outgasing the sample holder. The analysis chamber is for the ultimate analysis measurement.

After the light is monochromatized, it is then introduced into the analysis chamber which is equipped with essential surface analytical apparatuses. The analysis chamber was designed by Dr. J. R. Anderson of Montana State University. The system layout is shown in Fig. 11.

The analyzer used for photoelectron diffraction measurement is a hemispherical analyzer of 50 mm spherical radius (HA-50) made by Vacuum Science Workshop (VSW), and is mounted on a goniometer with two axial rotation motions (see Fig. 12). The analyzer aperture is 1 mm in diameter (acceptance half-angle about 1°) to assure angle-resolved measurement.

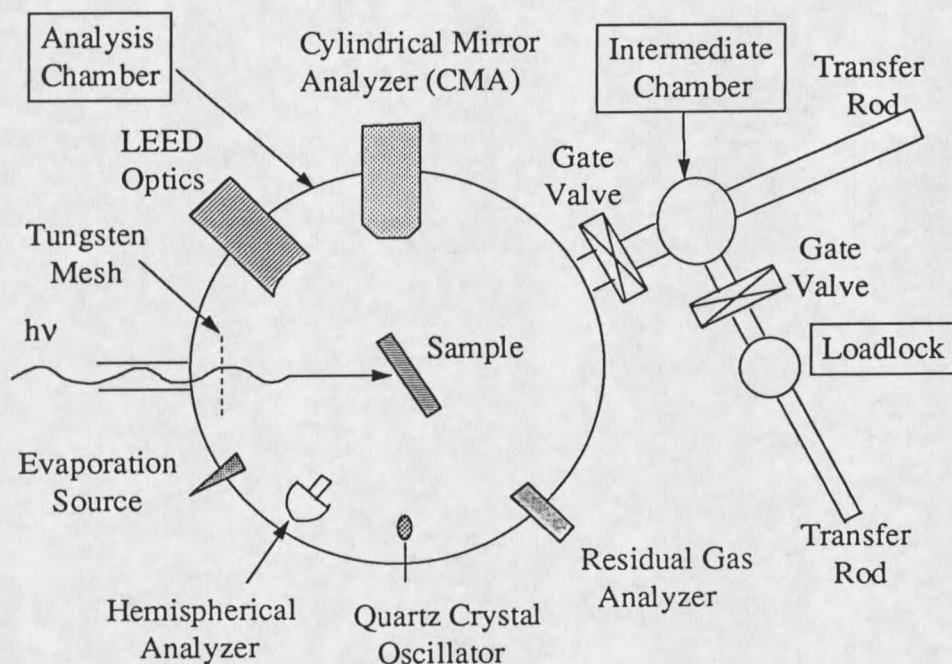


Fig. 11. Schematic layout (top view) of vacuum systems: Analysis Chamber, Intermediate Chamber, and Loadlock.

The system is also equipped with a double pass cylindrical mirror analyzer (CMA) mounted in the horizontal plane. Its axis intersects the incident beam at the center of the chamber and 90° with respect to the horizontal projection of the incident light. CMA has larger acceptance angle (acceptance cone angle 12°) so it is ideal for high resolution core level studies. Low Energy Electron Diffraction (LEED) optics is used for surface reconstruction studies. LEED pattern reflects the long range order of the surface, which is a great help to determine the surface/interface structure. The evaporation source is loaded with materials needed to be deposited onto the sample. A quartz crystal oscillator (QCO) is used for monitoring the deposition process. The residual gas analyzer is used for monitoring the residual gas components inside the chamber, which is very useful for

In above figure, the sample is mounted on a manipulator (not shown) with three linear motions (x , y , z) and two axial rotation motions (ϕ , φ). The coordinate system is defined as follows: the origin o is the point at which the incident beam strikes the sample surface, x is against the beam's horizontal projection, y is perpendicular to x in the horizontal plane, and z is in the vertical direction. The incident plane contains the beam, x , and z . The beam has an incident angle δ ($\sim 2^\circ$) relative to the horizontal. The horizontal plane contains x , n , y' , y , and t , where n is the sample normal, y' is the zero axis of the goniometer, and t is sample's horizontal axis in the surface plane. The manipulator's φ motion rotates the sample about its normal, and the ϕ motion rotates the sample about z axis (*i.e.* rotates the sample normal n away from x axis).

The HA-50 analyzer is mounted on the goniometer which is attached vertically on the turntable. The goniometer can swing the HA-50 up and down in vertical plane, which changes HA-50's vertical acceptance direction ψ . The turntable can also spin HA-50 about the vertical axis, which changes HA-50's horizontal direction θ .

In the final measurement state, the center of goniometer is tuned to coincide with the hitting point of incident beam on the sample surface, and the turntable is also need to be level with the horizontal plane. In the actual measurement, ϕ is fixed (62.5°), ψ is fixed (0° , *i.e.* HA-50 is in the horizontal plane), θ runs from 0° to 90° , and φ runs from 0° to 360° .

Sample Preparation

The substrate was an n-type (phosphor doped, 0.1 - 10 Ω cm) Si (100) wafer with 4° vicinal cut along [110] direction. It was cut from a 2" wafer of 0.012" thickness to a 0.65" x 0.25" rectangular shape. The Si substrate is mounted on a sample holder and then loaded into the loadlock from air. The loadlock is then pumped down. After the pressure is better than 1×10^{-5} torr, it is transferred into the intermediate chamber where the base pressure is about 5×10^{-10} torr. Then the Si substrate is heated to 500°C by direct heating (*i.e.* passing electric current though the sample directly) for several hours. This process is to outgas the sample holder to obtain a clean surrounding. When the pressure in the intermediate chamber is better than 1×10^{-9} torr, the sample is transferred into the analysis chamber where the base pressure is $5-7 \times 10^{-11}$ torr. The Si substrate is then heated to 1150°C for 10 sec to burn off silicon oxide layers. A 2x1 single domain dominant LEED pattern is obtained.

The preparation of selenium on Si(100) is as follows. A piece of ZnSe single crystal is loaded in the evaporation source cell which is made of tantalum foil of 0.002" thickness and shaped like a boat. A K-type thermocouple is spot-welded onto the evaporation source cell to monitor the source temperature. Then a current is passed through the source to heat it. Before the deposition, the source must be outgassed in order to obtain a clean deposition. The outgas process is a time-consuming job. The source has to be heated up slowly while maintaining the pressure within 10×10^{-10} torr. When the source temperature is approaching 900°C, the pressure is kept better than 2×10^{-10} torr. At this temperature, the source evaporates Zn and Se atoms. After certain deposition time (about 3 to 5 min.), the Si substrate is covered by Zn and Se. Then the sample is annealed

to 550°C. During this annealing process, Zn is removed and surface is covered with Se. LEED shows a 1x1 pattern. The Si(100)-Se:1x1 system is then prepared.

The preparation of aluminum on Si (100) is not trivial, mainly because the outgasing of aluminum source is extremely difficult. Several attempts of making a working aluminum source were tested before a workable one was found. This source is made as follows. First, a basket is made with tantalum wire of 0.02" in diameter. Then, a piece of aluminum wire is curled and loosely packed into it. The basket can only be half-filled. Now a current is run through the basket to heat the aluminum. When the aluminum is just at melting point (660°C), the heating current is precisely controlled to let aluminum just flow and coat the tantalum basket wire. The conductance will have changed (increased) in the process so that a higher current is more likely needed in order to evaporate aluminum out. Here, patience plays an important role. The outgasing must be done in cycles, *i.e.* heating up the source and cooling it down, until the deposition rate is stable and the evaporation pressure is kept better than 2×10^{-10} torr. At this time, the aluminum source is clean and ready for use. During the aluminum deposition, the Si substrate is kept at 100°C. The deposition process is completed after a well ordered 2x2 LEED pattern is formed. Thus the Si (100)-Al:2x2 system is prepared.

Magnesium on Silicon system is fairly easy to obtain. Magnesium evaporates at fairly low temperature (~ 350°C). A piece of bulk magnesium is placed into a tantalum boat. A K type thermocouple is spot-welded onto the tantalum boat for temperature monitoring. When the source has been successfully outgased, the deposition pressure is

kept under 1×10^{-10} torr. After the deposition of magnesium onto silicon substrate, the sample is annealed to 350°C . A 2×2 LEED pattern is formed. The Si (100)-Mg: 2×2 system is then made.

Data Acquisition

Data Acquisition System Setup

The data acquisition setup is shown in the following diagram, which basically shows the connections among the monochromator, the HA-50, and the computer controlled system.

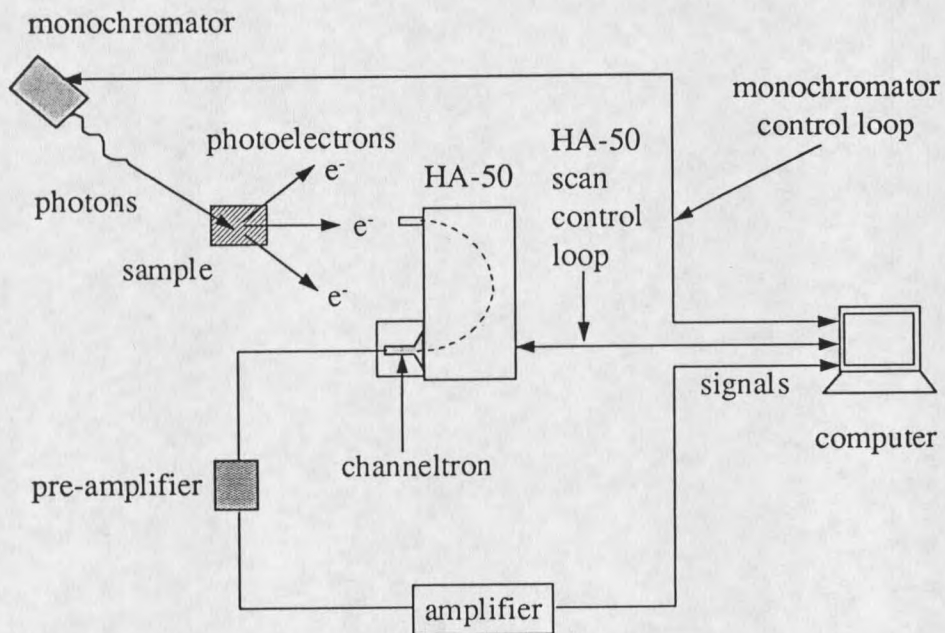


Fig. 13. Schematic diagram of the connections among the monochromator, HA-50, and computer controlled system.

In above figure, the monochromator control loop is for the selection of photon energy. It consists of 2 pairs of control cables. One pair is for ERG and the other one is for the Seya. The HA-50 scan control loop connects the computer to HA-50. After the photon energy is selected, the computer sends out kinetic energy scan signals to HA-50 where to start the scan and where to end, and HA-50 responds accordingly. At the same time, photoelectron signals are multiplied by channeltron, then amplified by the pre-amplifier and the amplifier, and finally recorded by the computer to the corresponding kinetic energy. Thus an energy distribution curve (EDC) is obtained (see Fig. 14).

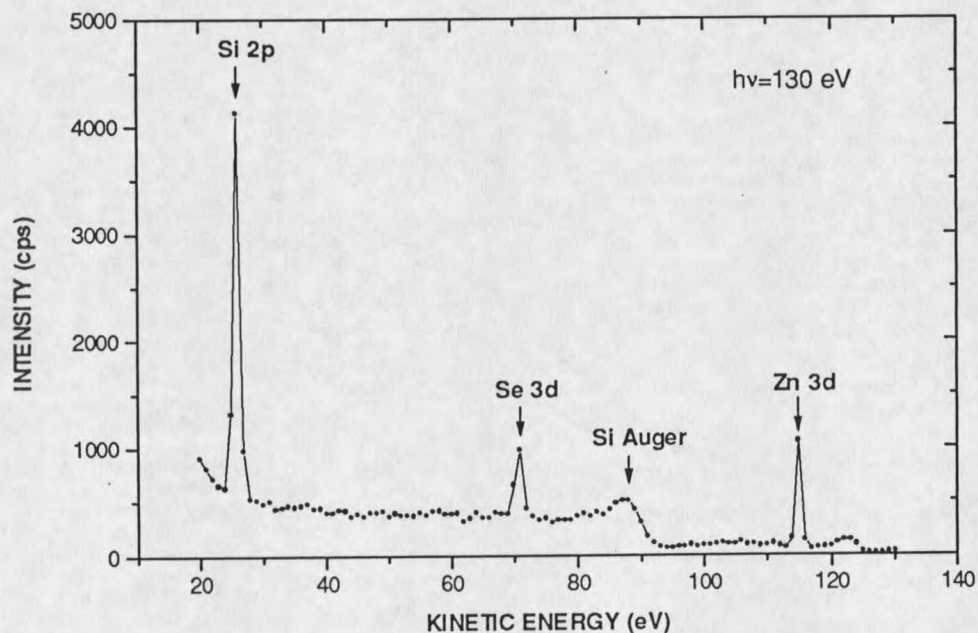


Fig. 14. EDC wide scan of ZnSe/Si taken at room temperature (photon energy 130 eV).

Data Acquisition Procedures

The photoelectron holography data is achieved by obtaining a series of CIS spectra. As described in chapter 2, a CIS spectrum is a $I(k)$ (photoelectron intensity) vs. k (electron momentum) spectrum for a given initial state electron at a fixed emission angle.

As an example, in the case of Si(100)-Se:1x1 sample, a Se 3d EDC spectrum is measured at a certain photon energy (see Fig. 15) at a fixed emission angle.

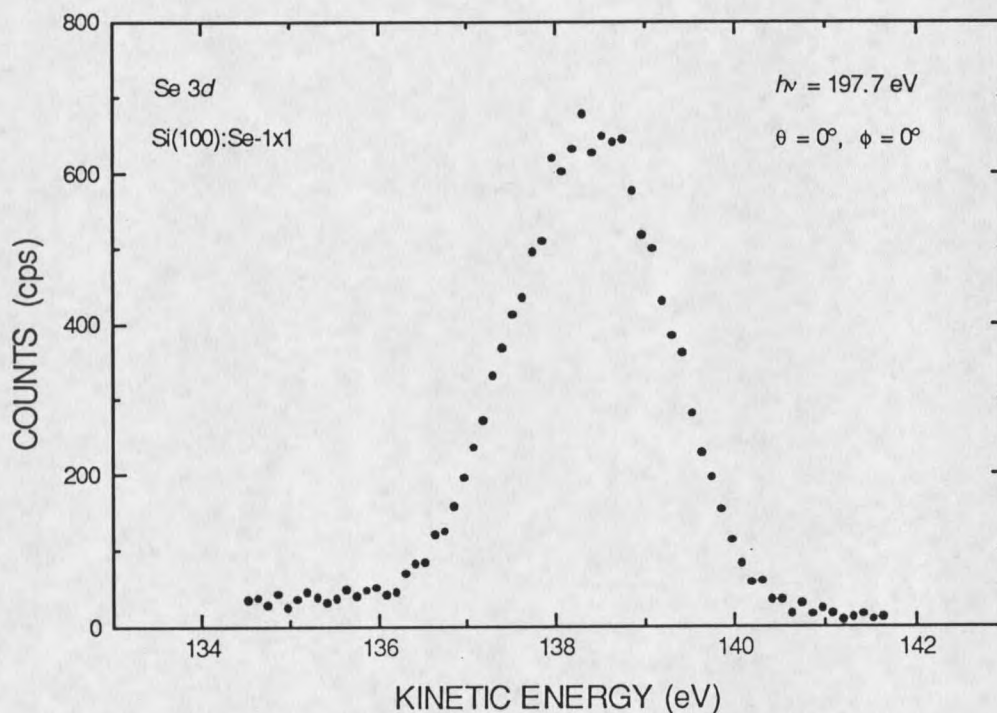


Fig 15. A typical EDC curve of Se 3d taken at normal emission direction.

The Se 3d signal intensity is calculated and normalized to the mesh current which is recorded at the same time when Se 3d EDC spectrum is measured. The Se 3d signal intensity and its electron wave number k value are stored. The electron wave number k is calculated by the following formula,

$$h\nu = \hbar^2 k^2 / 2m_e + E_b \quad (3.1)$$

which basically is the energy conservation law, where $\hbar = h/2\pi$, m_e is the electron mass, and E_b is the binding energy of a given initial state of the adsorbate.

When the first Se 3d EDC spectrum is finished and stored, the photon energy is then changed to another value, and the second Se 3d EDC starts, and so forth. After all the Se 3d EDC's are measured from the highest photon energy to the lowest photon energy, we have obtained a CIS spectrum by plotting out the Se 3d signal intensity vs. corresponding k value. In the following figure, a typical CIS spectrum is shown for the Se adsorbate of initial state 3d on Si (100) surfaces. The vertical coordinate represents Se 3d signal intensity, while the horizontal coordinate represents the electron wave number k .

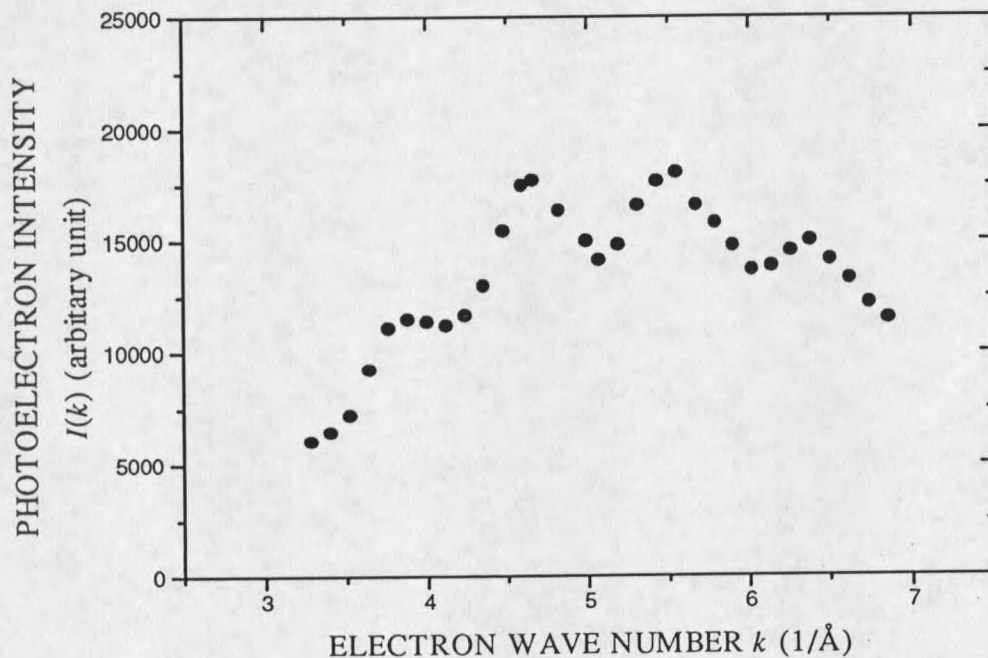


Fig. 16. A typical CIS spectrum of Se 3d taken at $\theta = 45^\circ$, $\phi = 50^\circ$ for Si(100-Se:1x1).

The CIS measurements were carried out at 95 different angles over the first quadrant ($\pi/4$ steradians) of the emission hemisphere (π steradians), which is an irreducible region (see Fig. 17). The Si(100)2x1 surface has two-fold rotational symmetry about the [001] direction and two mirror planes along two principal axes $[1\bar{1}0]$ and $[110]$. The CIS's are spread out in the space with equal solid angle spacing, *i.e.* 0.0083 steradians per CIS point. The polar angle spacing $\Delta\theta$ is kept constant (usually 7.5°). To ensure uniform distribution of the measuring positions in the emission hemisphere, the azimuthal angle spacing $\Delta\phi$ is then calculated by the following formula

$$\Delta\phi = \Delta\theta / \sin\theta. \quad (3.2)$$

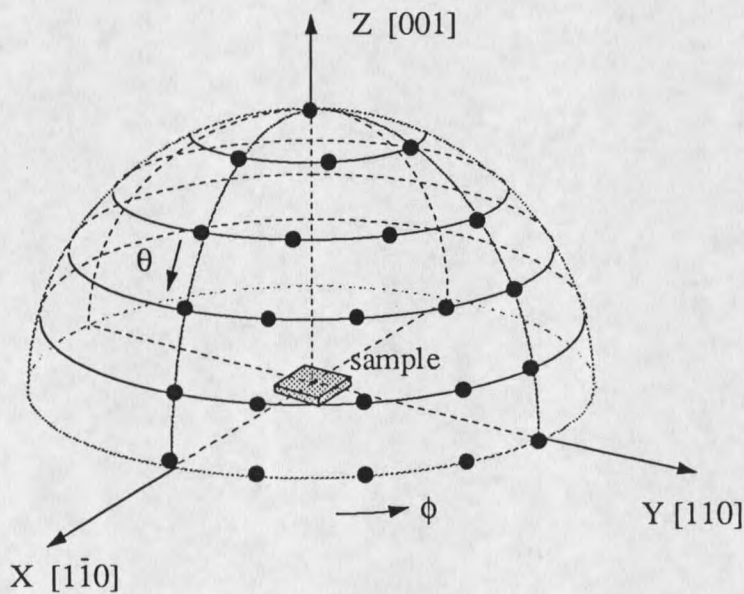


Fig. 17. Schematic drawing of the distribution of measured CIS positions in the first quadrant of the emission hemisphere.

The above figure is a demonstration of the distribution of the CIS positions in the first quadrant of the emission hemisphere defined by the positive directions of x, y, and z axes, which correspond to $[1\bar{1}0]$, $[110]$, and $[001]$ directions respectively.

Data Analysis

EDC Peak Fitting

The measured EDC spectra of the adsorbates are first fitted with Gaussian peaks and linear backgrounds as given in the following formula:

$$Y^i(E^i) = Y_0^i e^{-((E^i - E_0^i)/\Gamma_i)^2} + (B_0^i + B_1^i E^i), \quad E^i \in (E_s^i, E_e^i) \quad (3.3)$$

where the index i stands for the i th EDC curve in a CIS spectrum, $Y^i(E^i)$ is the EDC count rate normalized to the mesh current, E^i is the scan energy argument starts at E_s^i and ends at E_e^i , Y_0^i is the peak count rate, E_0^i is the peak position, Γ_i is the peak width, B_0^i and B_1^i are the coefficients for the linear background function.

The integration of the i th EDC's Gaussian peak over the scanned energy range will give us the signal intensity $I(k_i)$ at k_i , *i.e.*

$$I(k_i) = \int_{E_s^i}^{E_e^i} Y_0^i e^{-((E^i - E_0^i)/\Gamma_i)^2} dE^i \quad (3.4)$$

where k_i and E_0^i satisfy the following condition,

$$h\nu_i = \hbar^2 k_i^2 / 2m_e + E_0^i \quad (3.5)$$

where $h\nu_i$ is the photon energy used for the i th EDC.

Repeating operation (3.5) for all the k_i 's (from k_{\min} to k_{\max}), we obtain a CIS spectrum with discrete points as shown in previous figure, where k_{\min} is the lowest electron wave number and k_{\max} is the highest.

CIS Inversion and Image Transform

The discrete CIS spectrum is spline-fitted to obtain a continuous $I(k)$. A non-diffractive curve $I_0(k)$ is generated for each CIS from the given data using a spline smooth routine in GENPLOT.³¹ Fig. 18 shows the original data points, $I(k)$ and $I_0(k)$.

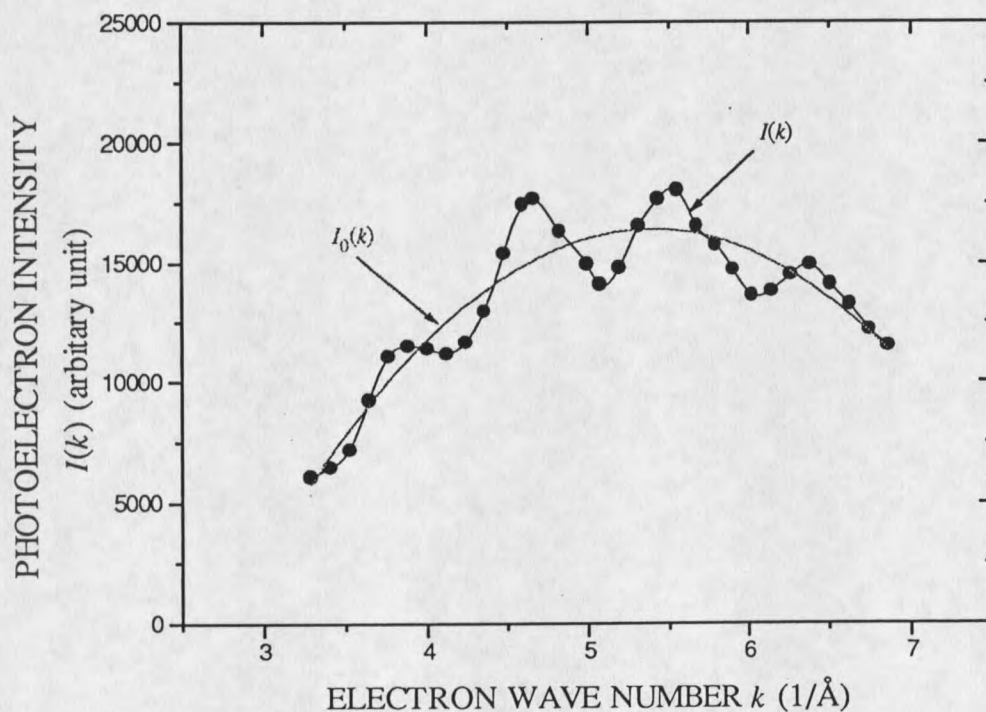


Fig. 18. A CIS Spectrum $I(k)$, and a non-diffractive reference curve $I_0(k)$ of Se 3d taken at $\theta = 45^\circ$, $\phi = 50^\circ$ for Si(100)-Se:1x1.

The $I_0(k)$ curve is used as a reference in the calculation of the normalized diffraction curve $\chi(k)$ (see Fig. 19), which is obtained by the following operation (cf. Eq.(2.85))

$$\chi(k) = I(k) / I_0(k) - 1. \quad (3.6)$$

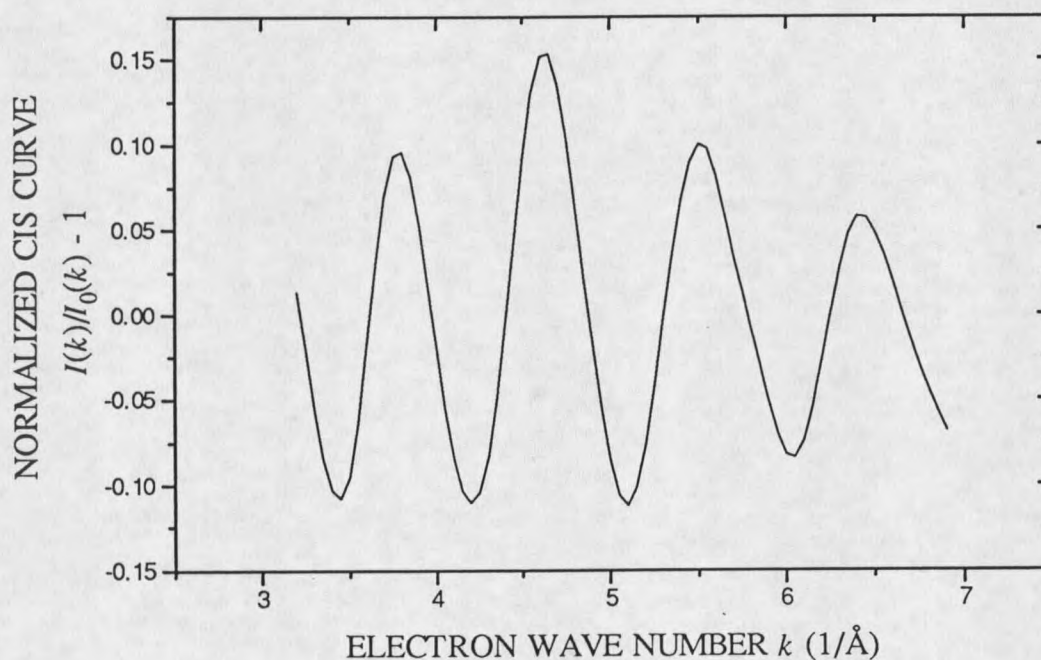


Fig. 19. The normalized diffraction curve $\chi(k)$ of Se 3d at $\theta = 45^\circ$, $\phi = 50^\circ$ for system Si(100)-Se:1x1.

Repeating operation (3.6) for all the CIS's, a series of $\chi(k)$ curves are obtained for the first quadrant of the emission hemisphere. The $\chi(k)$ curves are then mapped to the whole emission hemisphere according to the symmetry of the sample system.

The normalized $\chi(k)$ curves are then inverted to the transform function $\Phi(\hat{\mathbf{k}}, \mathbf{R})$ (cf. Eq. (2.88))

$$\Phi(\hat{\mathbf{k}}, \mathbf{R}) = \int_{k_{\min}}^{k_{\max}} \chi(\hat{\mathbf{k}}, k) e^{-ikR} e^{ik \cdot \mathbf{R}} g(k) dk \quad (3.7)$$

where $g(k)$ is the transform window function for reducing the noise near k_{\min} and k_{\max} . In this work, $g(k)$ is chosen to be the Hanning function which is given in formula (2.89).

During the transform, the inner-potential effect needs to be considered (cf. Chapter 2). The measured wave vector is actually in the vacuum side. The wave vector \mathbf{k} in the above transform integral (3.6) is actually inside the sample. If k denotes the electron wave vector inside the sample and k' for outside the sample (vacuum side), the relationship between these two quantities are given by Eqs (2.2a), (2.2b), and (2.3). Rewriting them in a spherical coordinate system, we have

$$k = (k'^2 + 2m_e V / \hbar^2)^{1/2} \quad (3.8a)$$

$$\theta = \sin^{-1}[(k' \sin \theta') / k] \quad (3.8b)$$

$$\phi = \phi' \quad (3.8c)$$

where $\mathbf{k}=(k, \theta, \phi)$, $\mathbf{k}'=(k', \theta', \phi')$ in spherical coordinate system, and $V=10$ eV in this work.

Finally, the image function $U(\mathbf{R})$ is constructed in the form of Eq. (2.117) using small-cone method. Inside the cone, a coordinate system is set up with the cone axis to be the polar axis denoted by z' . The polar angle of the cone coordinates is denoted by α , with its direction being the same as that of θ . The azimuthal angle of the cone coordinates is denoted by β . For a given direction (θ_c, ϕ_c) of the cone axis, the transformation matrix

from the small-cone coordinate system to the emission hemisphere coordinates is given below

$$\underline{M} = \begin{pmatrix} \cos \phi_c & -\sin \phi_c & 0 \\ \sin \phi_c & \cos \phi_c & 0 \\ 0 & 0 & 1 \end{pmatrix} \begin{pmatrix} \cos \theta_c & 0 & \sin \theta_c \\ 0 & 1 & 0 \\ -\sin \theta_c & 0 & \cos \theta_c \end{pmatrix}. \quad (3.9)$$

The unit vector \mathbf{x}' in the direction (α, β) in the small-cone coordinate system is given as follows

$$\mathbf{x}' = (\sin \alpha \cos \beta, \sin \alpha \sin \beta, \cos \beta). \quad (3.10)$$

The corresponding unit vector \mathbf{x} in the emission hemisphere system has the following relationship with \mathbf{x}'

$$\mathbf{x} \equiv (x, y, z) = \mathbf{x}' \underline{M}^T \quad (3.11)$$

where \underline{M}^T is the transpose matrix of \underline{M} .

Thus we have obtained the angle relationship between the small-cone coordinates and the emission hemisphere coordinates as given below

$$(\theta, \phi) = (\cos^{-1}(z), \tan^{-1}(y/x)) \quad (3.12)$$

with

$$x = (\cos \theta_c \sin \alpha \cos \beta + \sin \theta_c \cos \alpha) \cos \phi_c - \sin \alpha \sin \beta \sin \phi_c, \quad (3.13a)$$

$$y = (\cos \theta_c \sin \alpha \cos \beta + \sin \theta_c \cos \alpha) \sin \phi_c + \sin \alpha \sin \beta \cos \phi_c, \quad (3.13b)$$

$$z = (-\sin \theta_c \sin \alpha \cos \beta + \cos \theta_c \cos \alpha). \quad (3.13c)$$

Since the small-cone moves in the space during the image transform, only those CIS's inside the cone need to be inverted to ensure the same angular distribution of the CIS's used for all the small cones. To accomplish this, a set of angles (α_i, β_j) are chosen, in the

small-cone coordinate system with its cone axis in the direction (θ_c, ϕ_c) , by keeping $\Delta\alpha_i$ constant while $\Delta\beta$ is changed as $\Delta\alpha_i/\sin\alpha_i$. Thus formulas (3.12) and (3.13) are used during the image transform for such purpose, *i.e.*

$$(\theta_i, \phi_j) = (\cos^{-1}(z_{ij}), \text{tg}^{-1}(y_{ij}/x_{ij})) \quad (3.14)$$

with

$$x_{ij} = (\cos\theta_c \sin\alpha_i \cos\beta_j + \sin\theta_c \cos\alpha_i) \cos\phi_c - \sin\alpha_i \cos\beta_j \sin\phi_c, \quad (3.15a)$$

$$y_{ij} = (\cos\theta_c \sin\alpha_i \cos\beta_j + \sin\theta_c \cos\alpha_i) \sin\phi_c + \sin\alpha_i \cos\beta_j \cos\phi_c, \quad (3.15b)$$

$$z_{ij} = (-\sin\theta_c \sin\alpha_i \cos\beta_j + \cos\theta_c \cos\alpha_i), \quad (3.15c)$$

Thus transformed image function is in discrete data form. It is then interpolated in three dimensional fashion by *Mathematica*^{®32} to form a continuous image function $U(\mathbf{R})$, from which various kinds of image plots are made. The image plots are also displayed by *Mathematica*[®] - a commercial software for scientific computation and graphical display.

CHAPTER 4

EXPERIMENTAL RESULTS AND DISCUSSION

In this chapter, the data are reported for three systems, Si(100)-Se:1x1, Si(100)-Al:2x2, and Si(100)-Mg:2x2, which have been investigated and the interfacial structures are obtained from the experimental results. Each of these three systems displays its unique structural features, as discussed in the following sections.

Si(100)-Se:1x1

The substrate is Si(100) with 4° miscut along [011] direction. The miscut sample is used to obtain a single-domain biatomic-step-height surface for clean silicon. After Si(100) is annealed to 1100°C , a 2x1 LEED pattern is observed as depicted in Fig. 20.

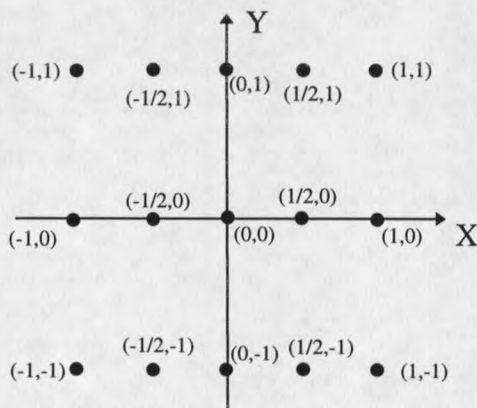


Fig. 20. Si(100)-2x1 LEED pattern after 1100°C annealing. The x-y plane is in the sample surface, while the x-axis is along the Si-Si dimer bond direction as will be seen in Fig. 21. The spots are labeled with indices for identification.

The 2×1 LEED pattern of the clean Si(100) surface is due to the reconstruction of surface Si atoms by forming Si-Si dimers which minimize the number of dangling bonds on the surface such that the surface energy is minimized. The Si dimer structure of the clean Si(100) surface is shown in Fig. 21.

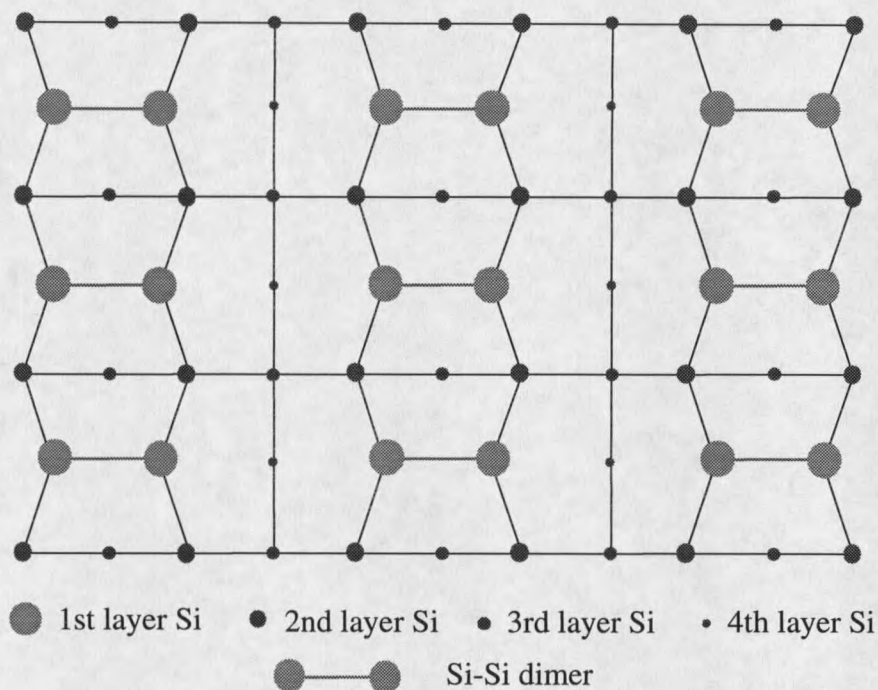


Fig. 21. Diagram of the reconstructed Si(100) surface. The top layer Si atoms form Si-Si dimer bonds to minimize surface energy.

After the selenium-adsorbed silicon surface was prepared, as described in the "sample preparation" section of chapter 3, the surface structure has changed from a single-domain (2×1) geometry of clean Si(100) to well-ordered (1×1) . Apparently, selenium completely removes the reconstruction formed by surface silicon dimers.

The atomic image obtained by the transform method described in chapter 2 shows that Se adsorbates occupy the bridge sites. Since the image function (*cf.* Eq.(2.118)) has

three position variables x , y , and z , the display of such image cannot be carried out in an ordinary two dimensional way. As the transform suggested, the intensity maximum positions of the image function correspond to the substrate atom positions in real space. By slicing the three-dimensional image and displaying the image intensity in two dimensional plot in gray-scale plot (*i.e.*, the darker the spot, the higher the intensity), we can examine the three-dimensional image and obtain the atomic positions. The two-dimensional image plot is often referred to as the "image cut". A horizontal or vertical cut means a two-dimensional image plot parallel or perpendicular to the sample surface.

Now, let us examine the Se image. Figure 22 is a horizontal cut of the image function at $Z = -1.1 \text{ \AA}$. Intensity maxima labeled by A, B, A', and B' are due to first-layer Si atoms from double-domain surfaces. Labels with no prime represent the contribution from domain I in which Si-Se-Si bonding plane (*i.e.*, the plane containing Se and two bonded Si atoms) is parallel to the step edges, and labels with primes represent domain II in which Si-Se-Si bonding plane is perpendicular to the step edges (see Fig. 28(b)). Domain I has 90° rotation with respect to domain II. Figure 23 is another horizontal cut at $Z = -2.4 \text{ \AA}$. There are four intensity maxima marked by C/F', D/C', E/D', and F/E'. The label C/F' means C and F' coincide at the same place (such definition applies to the whole discussion unless otherwise noted). The four intensity maxima are due to second-layer Si atoms. Figures 24 and 25 display the horizontal image cuts passing through the third and the fourth Si layers respectively. The intensity values for the nearest Si atoms are the strongest and are normalized to 100. The intensity values for the second-, third-, and fourth-nearest Si atoms are 12, 3, and 4 respectively. Figure 26 is an X-Z vertical

planar cut at $Y=0$. In panel (a), there are two intensity maxima labeled by A and B which are due to the first layer Si atoms. The Se emitter is at the center of the cross. This clearly show Se adsorbate occupies the bridge site. The first-layer Si atoms (A and B) show the strongest intensity while the third- (G' and H') and fourth- (J/J') layer Si atoms are barely seen in panel (a). After intensity magnification by a factor of 35, the third- and fourth-nearest Si atoms show the same plotting intensity in panel (b) as that of the nearest Si atoms in panel (a). The same characteristic can be seen in Fig. 27, which is a Y-Z vertical planar cut at $X=0$.

Fig. 28(a) is a three-dimensional diagram based on the image results. Fig. 28 (b) and (c) are the decomposed structures for Se1 and Se2, which belong to two different domains.

The image plots clearly show that (1) Se adsorbates occupy the bridge sites, and (2) two adsorption domains are formed on the surface. Fig. 29(b) is a schematic drawing of Se-adsorbed two-domain surfaces. To begin with, clean Si(100) surfaces present a single-domain 2×1 LEED patterns, as a result of the formation of the biatomic-step surfaces and the Si dimer bonds parallel to the step edges (see Fig. 29(a)).³³ If Se adsorbates occupied only the bridge sites, the image plots would have only shown intensity maximum positions marked by the labels with no primes. The emergence of Se-adsorbed two-domain surfaces indicates that the Si surfaces have undergone through a rearrangement during the adsorption process.

Early studies of Se on Si(100) have found that surface etching can occur during the Se deposition process.^{9 34} Following this argument, it can be assumed that etching has

occurred on the Si surfaces, changing them from a double-step configuration to that of a single-step (monatomic step), which manifests double-domain structures.

A model is proposed for such domain change during the Se adsorption process (see Fig. 30). At 550°C, surface Si atoms are very mobile. With the assistance of Se, a quarter of the Si atoms (shaded area in Fig. 30(a)) on the upper terrace move down to the lower terrace to form double domain surfaces, followed by the adsorption of Se on the rearranged Si surfaces. The terrace width of a double domain surface (Fig. 30(b)) is only half of that of a single domain surface. For the 4° miscut Si(100) surface, the former is about 19Å, and the latter is about 38Å.

The atomic positions and image intensities of Si scatterers are listed in Table 1. Theoretical calculations of Si atomic positions are also listed. It can be seen that positions obtained from experimental results and theoretical calculations are in good agreement.

Table 1. The atomic positions and image intensities of Si atoms of Si(100)-Se:1x1. The origin is at the Se emitter, the x-axis is along $[1\bar{1}0]$ parallel to the step edges, and the y-axis is along $[110]$ perpendicular to the step edges.

Si Atom Labels	Corresponding Si layer	Image Intensity	Atomic Position (Å)	
			Experiment	Theory ⁸
A	first	90	(-1.7, 0, -1.1)	(-1.899, 0, -1.265)
B	first	90	(1.7, 0, -1.1)	(1.899, 0, -1.265)
A'	first	100	(0, -1.8, -1.1)	(0, -1.899, -1.265)
B'	first	100	(0, 1.8, -1.1)	(0, 1.899, -1.265)
C/F'	second	12	(-2.0, 1.9, -2.4)	(-1.899, 1.899, -2.668)
D/C'	second	12	(-1.9, -2.0, -2.4)	(-1.899, -1.899, -2.668)
E/D'	second	12	(1.8, -1.9, -2.4)	(1.899, -1.899, -2.668)
F/E'	second	12	(1.8, 1.9, -2.4)	(1.899, 1.899, -2.668)
G	third	3	(0, 1.8, -3.8)	(0, 1.899, -4.022)
H	third	3	(0, -2.1, -3.6)	(0, -1.899, -4.022)
G'	third	4	(-2.0, 0, -3.6)	(-1.899, 0, -4.022)
H'	third	4	(-1.8, 0, -3.8)	(1.899, 0, -4.022)
J/J'	fourth	4	(0, 0, -5.1)	N/A

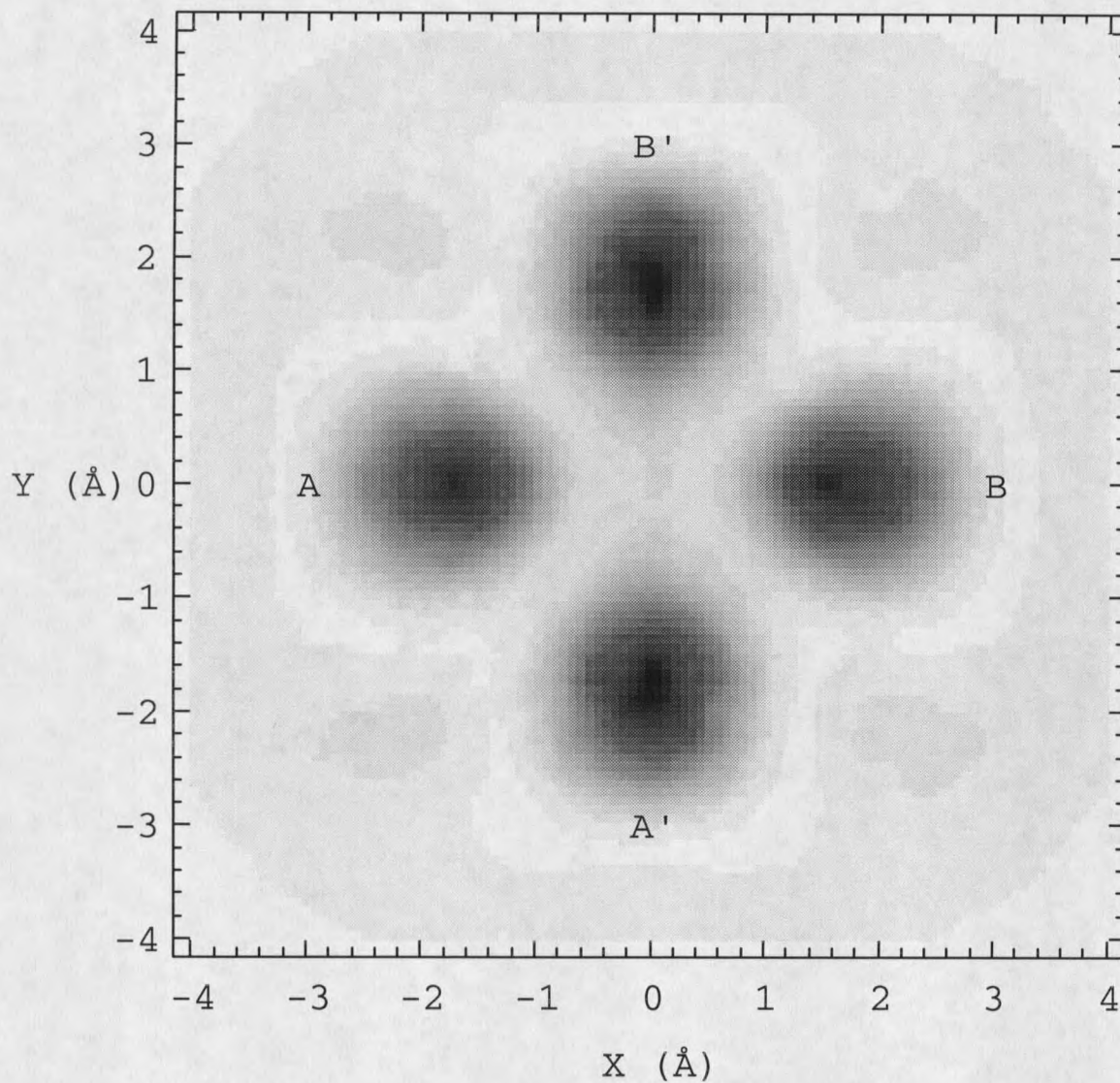


Fig. 22. X-Y horizontal planar cut of the image function at $Z = -1.1 \text{ \AA}$ for Si(100)-Se:1x1. Intensity maxima labeled by A, B, A', B' are due to first-layer-Si atoms of two domains (A and B for domain I, and A' and B' for domain II). The intensity maxima values are 100. The x-axis is along the $[1\bar{1}0]$ direction parallel to the step edges, and the y-axis is along $[110]$ perpendicular to the step edges. This coordinate convention applies to the rest of the discussion, unless otherwise noted.

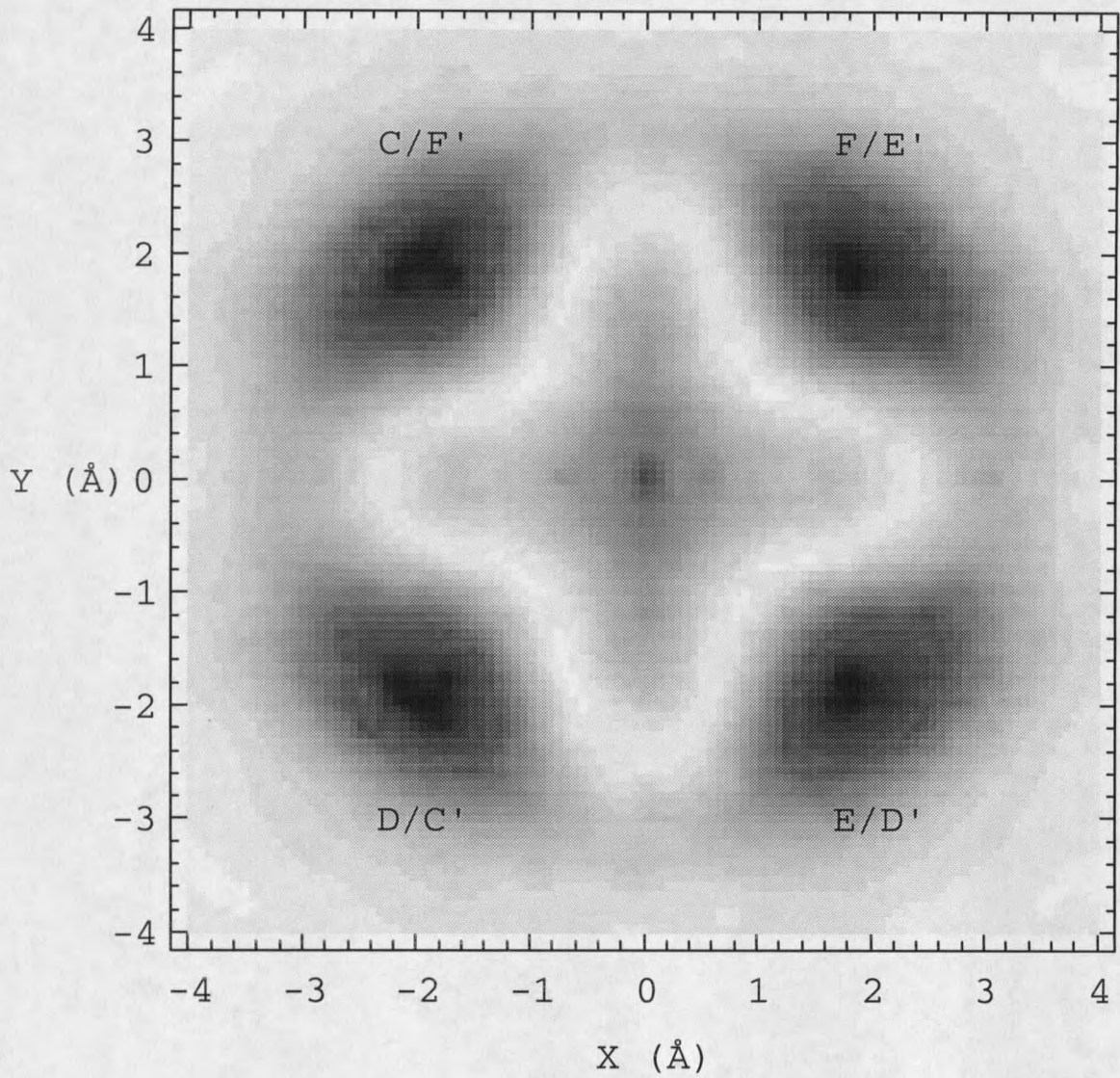


Fig. 23. X-Y horizontal planar cut of the image function at $Z = -2.4 \text{ \AA}$ for Si(100)-Se:1x1. Intensity maxima labeled by C/F', D/C', E/D', F/E' are due to second-layer Si atoms. The intensity values at the maximum positions are 12.

